NOTE TO USERS

Wavelet Domain Image Restoration using Adaptively Regularized Constrained Total Least Squares

Xiaojun Zhang

A Thesis

in

The Department

of

Electrical and Computer Engineering

Presented in Partial Fulfillment of the Requirements
For the Degree of Master of Applied Science at
Concordia University,
Montreal, Quebec, Canada

April 2005

Your file Votre référence
ISBN: 0-494-04408-X
Our file Notre référence
ISBN: 0-494-04408-X

ABSTRACT

Wavelet Domain Image Restoration using Adaptively Regularized Constrained Total Least Squares

Xiaojun Zhang

This thesis is concerned with image restoration techniques using adaptively regularized constrained total least squares (ARCTLS) and wavelet transforms. The objective of the thesis is to improve the conventional ARCTLS algorithm by exploiting the subband properties of both the degraded image and the point spread function (PSF) of the degradation system.

First of all, two most frequently used restoration algorithms, namely, the regularized constrained total least squares (RCTLS) and its adaptive version (ARCTLS) are investigated. The solutions of the two techniques in the DFT domain are emphasized in order to reduce the computational complexity. It is shown that both techniques are very suitable for the degradation situation where the (PSF) and the observed degraded image are subject to the same type of error. A new termination criterion is also proposed for the iterative ARCTLS algorithm to increase the convergence rate. Our simulation results show that the convergence speed using the proposed criterion is at least 20% faster than that used of the conventional ARCTLS method.

Secondly, a wavelet-domain image restoration technique using ARCTLS is presented.

The 1-D and 2-D wavelet transform matrix representations are formulated for both the degraded image and the degradation convolution operator. A class of orthonormal wavelet based quadrature mirror filter bank is investigated and applied to the subband decomposition of the degraded image and the PSF as well such that the conventional ARCTLS algorithm can be employed for each subband image restoration. The restored subband images are then reconstructed using the QMF to yield the complete restored image. Computer simulation of the proposed method is conducted based on some standard test images. The experimental results show that the proposed wavelet-domain ARCTLS (WARCTLS) technique outperforms the conventional ARCTLS in terms of the improved signal-to-noise ratio (ISNR) of the restored image.

ACKNOWLEDGEMENTS

It has been a great privilege for me to work with Dr. Wei-Ping Zhu, my research adviser and thesis supervisor, who has introduced me to the area of digital signal processing using wavelets and provided me an opportunity to pursue research in image processing. I am truly grateful for the insightful advice and the constructive criticism that he gave me and especially for his inspiration and confidence during the course of this work. This important collaboration has been, assuredly, one of the most enriched experiences in my life.

I would also like to express my sincere gratitude to Drs. E.I. Plotkin and William Lynch. I have the pleasure to study their courses and learned a lot from them, which gave me much knowledgeable introduction towards understanding and pursuing the task of this thesis.

I would also like to express my heartfelt appreciation to my father, my mother and my sister for their love and motivation.

I dedicate this work to the memory of my mother ...

Contents

LIST of Figures

List of Tables

List of Algorithms

List of Abbreviations

PSF	:	point spread function
FT	:	Fourier transform
HVS	:	Human visual system
AR	:	Auto-regressive
MAP	:	Maximun a posterior probability
MEM	:	Maximun entropy
RL	:	Richardson-Lucy
RCTLS	:	regularized constrained total least squares
CTLS	:	constrained total least squares
TLS	:	Total least squares
ARCTLS	:	adaptively regularized constrained total least squares
WT	:	wavelet transform
MRA	:	multi-resolution analysis
QMF	:	quadrature mirror filter
ISNR	:	improvement in signal-to-noise-ratio
DFT	:	discrete Fourier transform
FFT	:	fast Fourier transform
DWT	:	discrete wavelet transform

BSC	:	block-semi circulant
SBC	:	semi-block circulant
IID	:	independent identically distributed
AWGN	:	additive white Gaussian noise
BBSC	:	block-block semi-circumant
BSBC	:	block-semi block-circumant
WARCTLS	:	wavelet-domain adaptively regularized constrained total least squares

List of Symbols

$g(m,n)$	:	degraded image pixel in spatial domain
$h(m,n)$	:	spatial representation of the degradation function
$f(m,n)$	:	ideal image pixel in spatial domain
$\eta(m,n)$	:	additive random noise in spatial domain
$*$	:	convolution operator
$G(u,v)$	:	degraded image pixel in frequency domain
$H(u,v)$	:	frequency representation of the degradation function
$F(u,v)$	:	ieal image pixel in frequency domain
$N(u,v)$	:	additive random noise in frequency domain
$\varphi(x)$	:	scaling function
$\psi(x)$	:	wavelet function
W_N^{kn}, W_N^{-kn}	:	one dimensional wavelet transform and its inverse
V_j	:	MRA scaling subspace
W_j	:	MRA wavelet subspace
$\oplus$	:	mathematical union
$\langle .,. \rangle$	:	inner product
$h_0(n), h_1(n)$	:	analysis highpass and lowpass filters

$g_0(n), g_1(n)$	:	synthesis highpass and lowpass filters
$\mathbf{g}$	:	matrix of degraded image in spatial domain
$\mathbf{H}$	:	matrix of degradation function in spatial domain
$\mathbf{f}$	:	matrix of ideal image in spatial domain
$\mathbf{n}$	:	matrix of additive random noise in spatial domain
$\hat{\mathbf{h}}, \Delta\mathbf{h}$	:	known and the error (unknown) components of the PSF
σ_h^2, σ_g^2	:	variance of the error components of PSF and the observation image
$\mathbf{u}$	:	unknown normalized noise vector
$\mathbf{Q}$	:	regularization operator
$\mathbf{W}, \mathbf{W}^{-1}$	:	wavelet transform matrix and inverse transform matrix
$\mathbf{D}$	:	1-D deinterlacing matrix
$\mathbf{D}_2$	:	2-D deinterlacing matrix
$\otimes$	:	Kronecker product

Chapter 1

Introduction

1.1 General

It is known that humans receive the vast majority of their sensory inputs through visual systems. Vision is the most advanced of our senses and plays the key role in human being's life. Great efforts have been made to artificially enhance our visual systems. Eyeglasses, binoculars, telescopes, radar, infrared sensors, and photo-multiplies all function to improve our view of the world and the universe.

Digital imaging has been widely used in medicine, aerial space, law enforcement, national defense, and industrial applications. With the rapid development of digital techniques and devices, such as very powerful computers, the field of image processing has grown vigorously in the past decades. In addition to applications in medicine and the space program, digital image processing techniques now days are used in all aspects of our life. With the increasing use of digital cameras, scanners, and internet services, the topic of image processing and/or analysis can be carried out more easily and efficiently. For example, with remote image acquisition systems and the network technology, people can access to and process on-line image signals that are being captured far away, as required by remote medical diagnosis and remote sensing.

Millions of images might be created every day in different fields. However, many of the images may not be of good quality due to various reasons. For instance, they might be degraded by the defects of optical lenses, the nonlinearity of electro-optical sensors, the graininess of film material, the relative motion between an object and the camera, improper focus, atmospheric turbulence in remote sensing or astronomy, etc. It is, therefore, very important to develop image restoration/enhancement techniques such that the original or the undergrade images can be restored.

Image restoration, as a subfield of digital image processing, has been receiving a great deal of research attention over the past decades. The ultimate aim of image restoration is to find the best approximation of the original image from the degraded version. It usually involves some means of undoing a distortion that has been imposed, such as motion blur or film graininess. Although this reverse process cannot be perfectly completed in most cases, vast improvements on the restoration quality have been possible in some circumstances [1]. As an image restoration problem is usually ill-conditioned, it in general lacks a unique solution. The number of possible solutions is limited only by human ingenuity. In this sense, the problem of image restoration results in an unmanageable and diverse field [2].

1.2 Brief Review of Image Restoration Techniques

1.2.1 Discrete Restoration Model

Image restoration can be modeled in different ways according to the specific type of

problem at hand. For example, it may be established as an inverse filtering problem if the degradation has been caused by a 2-D linear and space-invariant system. Furthermore, physical processes that govern image processing may make it possible to describe the degradation in a compact and specific manner such that a numerical/mathematical solution to the restoration problem can be found. Like most of the image restoration problems addressed in literature, we assume in this study that the degradation is caused by a linear space-invariant system and additive noise.

Figure 1.1 shows a model of the linear space-invariant degradation process with additive noise followed by a restoration process [3].

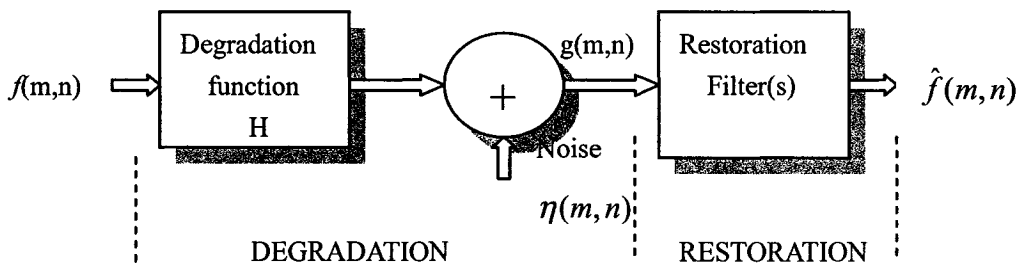

Figure 1.1 A model of image degradation/restoration process.

The degraded image can be expressed in the spatial domain as following

$$g(m,n) = h(m,n) * f(m,n) + \eta(m,n)$$
$$= \sum_i \sum_j h(m-i, n-j) f(i,j) + \eta(m,n) \qquad \textbf{(1.1)}$$

where *g(m,n)* is the degraded image, *h(m,n)* the spatial-domain representation of the degradation function/process, commonly referred to as the point spread function (PSF) of the degradation system, *f(m,n)* the original/ideal image, and $\eta(m,n)$ a random additive noise process. The symbol "*" denotes the convolution operation. Equation (1.1) can be

rewritten equivalently in the frequency domain as

$$G(u,v) = H(u,v)F(u,v) + N(u,v) \tag{1.2}$$

where u, v are the spatial frequency variables, and the capital letters *G, H, F* and *N* represent the Fourier transforms (FT) of the lower-case counterparts in (1.1). The restoration problem is to find an estimate of the original image *f(m,n)* or its FT through mathematical or optimization means either in the spatial or in the frequency domain.

1.2.2 Typical Image Restoration Techniques

1.2.2.1 Commonly Used Restoration Techniques

Image restoration techniques can be divided into two categories: deterministic methods and stochastic techniques. Generally speaking, deterministic methods are applicable to images with little noise and known degradation function. Stochastic techniques, usually giving better restoration results, seek to minimize some statistical error measurements such as the total mean squared error between the original image and the degraded one. Stochastic techniques also need some knowledge about the degradation process but not necessarily the complete degradation function. Certainly, it is more advantageous if the degradation function in question is completely known [2]. However, in most practical applications, there is no sufficient knowledge available about the degradation, and very often an approximation or estimation of the unknown degradation model has to be performed. There are basically two methods for implementing such an estimation depending on whether a priori knowledge or a posteriori knowledge is employed. A priori

knowledge about degradation is often available in many applications. For instance, when an image is degraded by a relative motion of an object with respect to the sensor, the degradation model should contain the speed and direction information of the motion of a capturing device such as a TV camera. The nature of the degradation remains unchanged during the motion period, and the speed and direction parameters can be estimated by studying a known sample image. Thus, the motion model and the parameters serve as a priori knowledge. On the other hand, a posterior knowledge can usually be obtained by analyzing a degraded image [4].

Most of the existing restoration techniques have attempted to use a priori knowledge of the degradation process for recovering the original image. This class of restoration methods is considered to be degradation model oriented. Based on the model used to introduce a priori knowledge, restoration algorithms may further be classified into two categories, namely, algorithms using space-invariant (stationary) models and those using space-variant (nonstationary) models. The use of stationary image models has been widely considered since these models can simplify the computational complexity of many restoration algorithms. However, the space-invariant assumption is not always true for images in real world. Therefore, many space-variant image restoration algorithms have been proposed in literature. Some examples include the algorithms that exploit the properties of the human visual system (HVS), and the recursive algorithms employing the Kalman filter [5], [6], [7]. A local decision process has been proposed in [8] to switch between different auto-regressive (AR) models, capturing the orientation of the edges

present at different spatial locations. In [9], an AR model driven by a white noise has been used to model the residual image. A maximum a posterior probability (MAP) method has also been proposed for nonstationary images. In [9] and [10], doubly-stochastic Markov random fields were used to minimize the nonconvex objective function associated with the restoration problem.

Some linear space-invariant image restoration algorithms, including the maximum entropy algorithm (MEM) [11], the Richardson-Lucy (RL) algorithm [12], and the likelihood cross-validation algorithm [13], have been developed for restoring HVS images. The pseudo-inverse filter, the minimum mean-square-error filter or the Wiener filter, and the constrained total least squares (CTLS) filter, have also been used to solve the restoration problem under the framework of a linear space-invariant degradation model [11].

1.2.2.2 Techniques Used to Develop the Proposed Approach

In this subsection, a few restoration methods that are closely related to the proposed approach are reviewed. Because of the presence of noise, solving Equation (1.2) is usually an ill-posed problem, implying that the solution may not be existent, unique or stable. In recent years, a lot of research work has been done on image restoration, resulting in some efficient algorithms. In [14], Katsaggelos et al have proposed the idea of employing a regularization function for solving ill-posed problems, which is regarded as a very effective restoration method.

The regularized constrained total least-squares (RCTLS) algorithm using a

regularization function has proven more successful than the constrained total least-squares (CTLS) algorithm and the total least-squares (TLS) algorithm when both the point spread function (PSF) and the degraded image are subject to the same type of errors [14]. Since the selection of the regularization parameter in RCTLS is based on the visual inspection of individual restored result, it is actually a trial-and-error scheme and there is no guarantee to have a high-quality restored image. To solve this problem, some researchers have proposed adaptively regularized constrained total least-squares (ARCTLS) algorithm to improve the RCTLS [15].

Wavelet transform (WT) has been an important tool for mathematical analysis and has found a wide range of applications in recent years. The wavelet-based subband decomposition has been extensively used for image compression, transmission, as well as analysis. It can also be applied to image restoration. A wavelet-based restoration approach involves the decomposition of the degraded and the estimated images into multiple channels based on their local frequency contents. The decomposition can be carried out by using a filter bank derived from a wavelet transform. The restoration problem is then converted into that of each multi-channel image [16]. The advantages of using the multi-channel restoration approach can be summarized as follows [17]:

- It allows for the regularization of each channel separately by considering the local properties of both the image and the noise. It also offers the flexibility of incorporating the inter-channel relations into the restoration.

- It allows us to exploit a priori knowledge at various resolution levels. Since one has a higher confidence in the restoration of lower resolution features in comparison to finer resolution features, the wavelet enables the determination of the trade-off between the resolution and the accuracy directly at each resolution level. This makes it possible to incorporate the data and a priori information about the original image into the same restoration algorithm at different resolution levels, thus providing a natural environment for data fusion applications.

1.3 Objective and Organization of the Thesis

It has been stated in the previous section that the RCTLS and ARCTLS algorithms can efficiently be applied to image restoration where both the PSF and the degraded image are contaminated by the same type of errors [14]. It has also been shown that the wavelet based subband approaches have become an appealing image restoration technique in recent years [18]-[20]. In this thesis, we attempt to develop the wavelet-domain ARCTLS restoration methods. To the best of our knowledge, the combination of ARCTLS and wavelets for image restoration has not yet been available in the literature. Our objective is to improve the conventional ARCTLS algorithm by exploiting the subband properties of both the PSF and the degraded image.

The rest of the thesis is organized as follows. In Chapter 2, some background material on wavelet theory is presented including the multi-resolution analysis (MRA) concept of signal/image, the advantages of using wavelets as well as the most commonly employed

fast discrete wavelet transforms based on orthonormal wavelet families. Quadrature mirror filters (QMF) which are based on orthonormal wavelet basis with compact support are also reviewed.

In Chapter 3, the matrix structures of multichannel linear filtering are described, followed by a brief discussion of the regularized constrained total least-squares (RCTLS) restoration algorithm with an emphasis on the adaptively RCTLS (ARCTLS) scheme. A strategic solution to the ARCTLS problem in DFT domain is derived. A new termination criterion with appropriate matrix-vector norms is also proposed to improve the convergence speed. The RCTLS and ARCTLS algorithms are computer-simulated to show the restoration results for different test images.

Chapter 4 presents the proposed image restoration methodology using the wavelet-domain adaptively regularized constrained total least-squares (WARCTLS). Both one-level and two-level wavelet decomposition matrices are applied to the input image and the point spread function (PSF) as well in order to obtain the subband coefficients. It is shown that a separable two-level decomposition matrix can easily be obtained from the one-level wavelet matrix. A simulation study of the proposed algorithm is conducted to confirm the superiority of the wavelet-domain ARCTLS over the two conventional CTLS methods without using the wavelet decomposition.

Finally in Chapter 5, some concluding remarks on the completed work and suggestions for future study are provided.

Chapter 2

Introduction to Wavelets

This chapter presents a brief review of wavelets and multi-resolution analysis of signals and images, including some fundamentals on wavelet transforms and the wavelet based filters. Detailed discussions in this regard can be found in [16]-[27].

2.1 General

Signal analysis is of crucial importance in many areas. The key idea of signal analysis is to decompose a signal, denoted as *f(x),* into a linear combination of expansion functions

$$f(x) = \sum_k a_k \varphi_k(x) \tag{2.1}$$

where a_k are real-valued coefficients, k an integer index of the finite or infinite sum, and $\varphi_k(x)$ the expansion functions. Then, the signal can be better analyzed/interpreted in terms of the expansion/basis functions φ_k. In many applications, *f(x)* can be expanded as a few terms only, if the coefficients a_k and a family of functions φ_k are properly chosen.

Fourier transform (FT) is the most commonly used transformation for signal analysis in signal and image processing field. The FT usually converts a signal from either the

time or the spatial domain into the frequency domain. According to the Fourier analysis, any signal/image can be expressed as the sum of a number (infinite or finite) of sine and cosine components. For a finite-duration signal or image *f(n)*, the discrete version of FT (DFT) is extensively used, which is defined as [28]

$$\text{Transform}: \quad F(k) = \sum_{n=0}^{N-1} f(n) W_N^{kn} \tag{2.2a}$$

$$\text{Inverse Transform}: \quad f(n) = \frac{1}{N} \sum_{k=0}^{N-1} F(k) W_N^{-kn} \tag{2.2b}$$

where, $W_N = e^{-j(2\pi/N)}$ and N is the length of the signal. The DFT is implemented, in general, by the fast Fourier transform (FFT). The computational complexity of FFT is $Nlog_2N$.

The Fourier representation reveals the global spectral content of a signal, but it cannot reflect some time-varying features of a signal during a particular period of time, or some local information in particular space coordinates in the description of images. Therefore, the Fourier representation is not capable of describing transient and nonstationary signals.

To facilitate the analysis of transient signals, i.e., to localize both the frequency and the time information of a signal, a number of basis functions have been proposed. More recently, wavelet transforms have been developed for the analysis and processing of signals and images. Wavelet transforms (WT) are based on small waves, called wavelets, of varying frequency and limited duration. This composition allows them to provide the equivalence of a musical score for an image, indicating not only what notes (or frequencies) to play but also when to play them. Some of the important features of

wavelets include the good decorrelation property and the sparse representation of images. Figure 2.1 shows the time-frequency tiles for FFT and a fast wavelet transform (FWT), where part (a) represents sampled data in the time-domain which provide no frequency information, part (b) represents a sinusoidal DFT basis in which no time resolution is reflected, and part (c) is an FWT basis which shows both time and frequency resolutions. It is also observed from Fig. 2.1 (c) that the time and frequency resolutions can be converted, namely, a better time resolution can be achieved at the expenses of sacrificing some frequency detail, vice versa. The main characteristics of wavelets that make them ideal for signal and image representation can be summarized as follows.

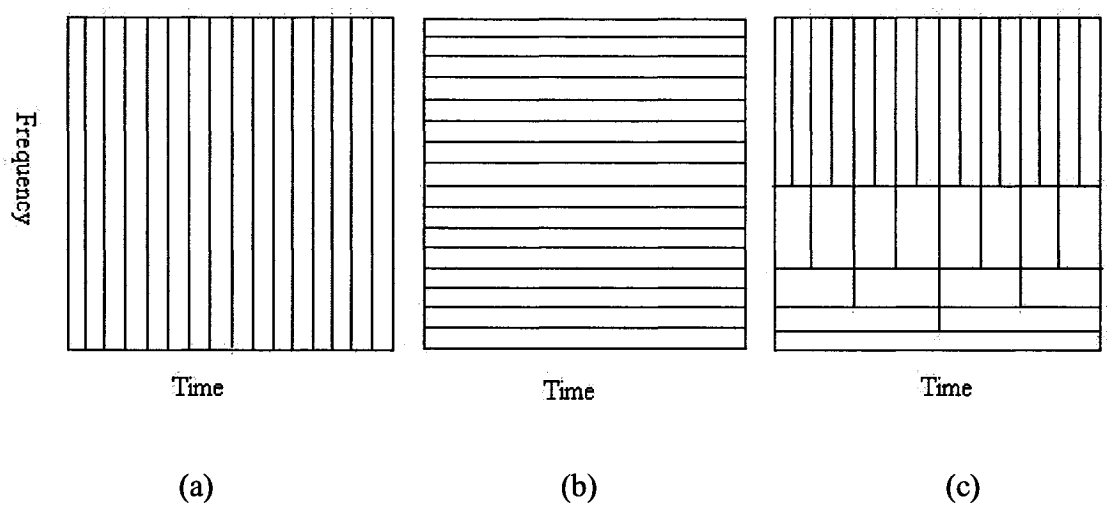

Figure 2.1 Time-frequency tiling for (a) sampled data (b) FFT, and (c) FWT.

1) Based on the multi-resolution concept, wavelets allow us to decompose and analyze a signal at different resolution levels (scales).

2) Wavelets have a good smoothness, which can be characterized by their number of

vanishing moments. A function defined on the interval [a, b] has n vanishing moments if

$$\int_a^b f(x)x^i dx = 0 \tag{2.3}$$

for i=0,1,…,n-1. The number of vanishing moments represents to what degree of smoothness a signal can be approximated on a wavelet basis.

3) There usually exist fast algorithms for the discrete wavelet transform such that the coefficients of the DWT and its inverse can be computed rapidly.

2.2 Multi-Resolution and Wavelets Analysis

2.2.1 Multi-Resolution Analysis

In multi-resolution analysis (MRA), a scaling function is used to create a series of approximations of a function, each differing by a factor of 2 from its nearest neighboring approximations. Additional functions called wavelets are then used to encode the difference in information between adjacent approximations.

Given a vector space $\mathbf{L}^2$ of the square integrable functions in $\mathbf{R}$, i.e.,

$$\mathbf{L}^2 = \left\{ f : \int_{-\infty}^{+\infty} f^2(x)dx < \infty \right\} \tag{2.4}$$

an MRA of $\mathbf{L}^2(\mathbf{R})$ is a sequence of closed subspaces $\{\mathbf{V}_j\}_{j\in Z}$ of $\mathbf{L}^2(\mathbf{R})$, satisfying the following properties:

1. $\mathbf{V}_j \subset \mathbf{V}_{j-1} \forall j \in Z$; (nesting property)
2. $\left(\bigcup_{j\in Z} \mathbf{V}_j\right) = \mathbf{L}^2(\mathbf{R})$; (density of the union in $\mathbf{L}^2(\mathbf{R})$)

3. $\bigcap_{j\in Z} \mathbf{V}_j = \{\mathbf{0}\}$;

4. $f(x)\in \mathbf{V}_j \Leftrightarrow f(2x)\in \mathbf{V}_{j-1}\forall j\in Z$; (scaling property)

5. $f(x)\in \mathbf{V}_0 \Rightarrow f(x-n)\in \mathbf{V}_0\forall n\in Z$; (invariance under integral translations)

6. $\exists\varphi\in \mathbf{V}_0 \ni \{\varphi_{0,n}\}_{n\in Z}$, is a Riesz basis of $\mathbf{V_0}$, where

$\varphi_{j,k}(x) = 2^{-j/2}\varphi(2^{-j}x-k)\forall j,k\in \mathbf{Z}$; (existence of a scaling function).

2.2.2 Scaling Function

According to the requirement for MRA, we can choose an appropriate scaling function φ_0 and then obtain $\mathbf{V}_0$ by taking the linear span of integer translation of φ. Other subspaces $\mathbf{V}_j$ can be generated as scaled versions of $\mathbf{V}_0$. Figure 2.2 shows the nested function space spanned by a scaling function

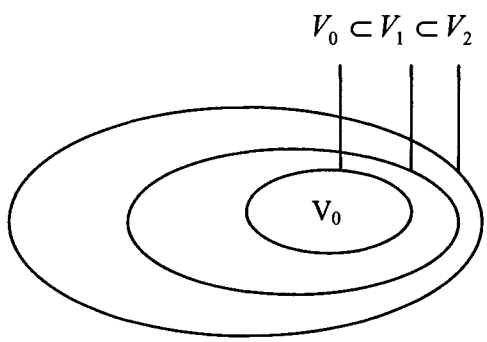

Figure 2.2 The nested function spaces spanned by a scaling function.

The real, square-integrable function set $\{\varphi_{j,k}(x)\}$ composed of integer translations and binary scaling is defined as

$$\varphi_{j,k}(x) = 2^{j/2}\varphi(2^j x-k) \tag{2.5}$$

for all $j,k \in \mathbf{Z}$ and $\varphi_x \in L^2(\mathbf{R})$. From these MRA properties, the expansion function of subspace $\mathbf{V}_j$ can be expressed as a weighted sum of the expansion functions of subspace $\mathbf{V}_{j+1}$. Finally, we can obtain a non-subscripted expression

$$\varphi(x) = \sum_n h_\varphi(n)\sqrt{2}\varphi(2x-n) \tag{2.6}$$

where the coefficients $h_\varphi(n)$ are called scaling function coefficients, which are often represented by a scaling vector $\mathbf{h}_\varphi$.

2.2.3 Wavelet Functions

The nested nature of the subspaces allows us to define a wavelet function ψ_x, which spans the difference between any two adjacent scaling subspaces, $\mathbf{V}_j$ and $\mathbf{V}_{j+1}$. The component of the wavelet function subspaces $\mathbf{W}_j$ is orthogonal to $\mathbf{V}_j$. The situation is illustrated graphically in Figure. 2.3.

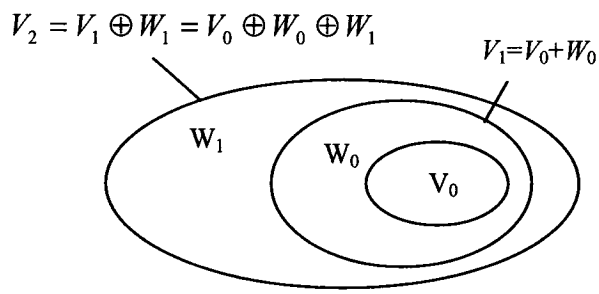

Figure 2.3 The relationship between scaling and wavelet function space.

If a set $\{\psi_{j,k}(x)\}$ of wavelets is defined as

$$\psi_{j,k}(x) = 2^{j/2}\psi(2^j x - k) \tag{2.7}$$

we obtain

$$\mathbf{V}_{j+1} = \mathbf{V}_j \oplus \mathbf{W}_j \tag{2.8}$$

$$< \varphi_{j,k}(x), \psi_{j,l}(x) >= 0 \qquad j,k,l \in \mathbf{Z} \tag{2.9}$$

We can also express the space of all measurable and square-integrable functions as

$$L^2(\mathbf{R}) = \mathbf{V}_0 \oplus \mathbf{W}_0 \oplus \mathbf{W}_1 \oplus \ldots = \mathbf{V}_1 \oplus \mathbf{W}_1 \oplus \mathbf{W}_2 \oplus \ldots \tag{2.10}$$

or

$$L^2(\mathbf{R}) = \ldots \oplus \mathbf{W}_{-2} \oplus \mathbf{W}_{-1} \oplus \mathbf{W}_0 \oplus \mathbf{W}_1 \oplus \mathbf{W}_2 \oplus \ldots \tag{2.11}$$

Any wavelet function, like its scaling function, can be expressed as a weighted sum of shifted double-resolution scaling functions, that is,

$$\psi(x) = \sum_n h_\psi(n) \sqrt{2} \varphi(2x - n) \tag{2.12}$$

where $h_\psi(n)$ are the wavelet function coefficients which can be written as a vector form, $\mathbf{h}_\psi$.

2.2.4 The Discrete Wavelet Transform (DWT) and Fast Wavelet Transform (FWT)

Like the discrete Fourier series expansion, the wavelet series expansion maps a discrete function *f*(n) into a sequence of coefficients. We define *N*-point discrete transform pair as

$$W_\varphi(j_0,k) = \frac{1}{\sqrt{N}} \sum_n f(n) \varphi_{j_0,k}(n) \tag{2.13}$$

$$W_\psi(j,k) = \frac{1}{\sqrt{N}} \sum_n f(n) \psi_{j,k}(n) \qquad j \geq j_0 \tag{2.14}$$

$$f(n)=\frac{1}{\sqrt{N}}\sum_{k}W_{\varphi}(j_0,k)\varphi_{j_0,k}(n)+\frac{1}{\sqrt{N}}\sum_{j=j_0}^{\infty}\sum_{k}W_{\psi}(j,k)\psi_{j,k}(n) \qquad \textbf{(2.15)}$$

where f(n), $\varphi_{j_0,k}(n)$, and $\psi_{j,k}(n)$ are functions of the discrete variable n=0,1,2,…,N-1. The coefficients $W_{\varphi}(j_0,k)$ in (2.13) and $W_{\psi}(j,k)$ in (2.14) are called approximation and detail coefficients, respectively.

The fast wavelet transform (FWT) is a computationally efficient implementation of the discrete wavelet transform (DWT) that exploits a very important relationship between the coefficients of the DWT at adjacent scales. The number of arithmetic operations, including multiplications and additions, is of *O(N)*. The wavelet-based filter bank algorithm is shown in Figure 2.4, in which the input signal *f(n)* is decomposed into two sub-bands via analysis filters h_0(n) and h_1(n) followed by a down-sampling process. The output signal, having the same resolution as the original one, is obtained by up-sampling and filtering the two subband signals (at a lower resolution) via the synthesis filters g_0(n) and g_1(n). Carefully designing the analysis and synthesis filters, the input signal can be reconstructed perfectly at the output.

Quadrature mirror filters (QMFs) have widely been used for speech and image coding [30]. A pair of low-pass and high-pass QMFs that are complementary in amplitude is often used for both analysis and synthesis purposes in a filter bank. A QMF bank not only satisfies the perfect-reconstruction property but also enjoys a low computational complexity due to its reduced number of independent coefficients. In order to implement a QMF bank, the filters in Figure 2.4 should satisfy the following conditions,

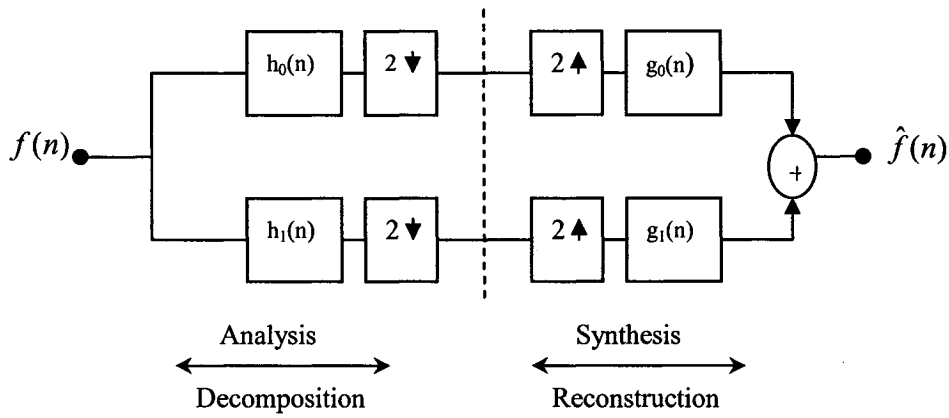

Figure 2.4 A two-channel filter bank for 1-D subband coding and decoding.

$$g_1(n) = (-1)^n g_0(2K-1-n)$$

$$h_i(n) = g_i(2K-1-n), \qquad \text{i}=\{0,1\} \qquad \textbf{(2.16)}$$

where h_i and g_i (i=1,2) are the impulse responses of the wavelet based analysis and synthesis filters. Examples of QMF banks include those designed by Daubechies [8], Smith and Barnwell [31], and Vaidyanathan and Hoang [32].

2.2.5 Two-Dimensional WT

One-dimensional wavelet transforms can easily be extended to the two-dimensional (2-D) case for a direct image transform in the 2-D spatial plane. A 2-D WT needs one separable scaling function $\varphi(x,y)$ and three 2-D separable wavelets, $\psi^H(x,y)$, $\psi^V(x,y)$, and $\psi^D(x,y)$, as given below

$$\varphi(x,y) = \varphi(x)\varphi(y) \qquad \textbf{(2.17a)}$$

$$\psi^H(x,y) = \psi(x)\varphi(y) \qquad \textbf{(2.17b)}$$

$$\psi^V(x,y) = \varphi(x)\psi(y) \qquad \textbf{(2.17c)}$$

$$\psi^D(x,y) = \psi(x)\psi(y) \qquad \textbf{(2.17d)}$$

Given separable 2-D scaling and wavelet functions, extension of the 1-D DWT to its 2-D counterpart is straightforward. One can simply take the 1-D FWT of the rows of *f(m,n)*, followed by the 1-D FWT on its columns. Similar to the 1-D filter bank algorithm, the 2-D FWT "filters" an image to generate four subimages, LL, LH, HL and HH, where the subimage LL is often referred to as the approximation and the other three as the detail of the original image. Figure 2.5 shows a block diagram for one-level decomposition of an image.

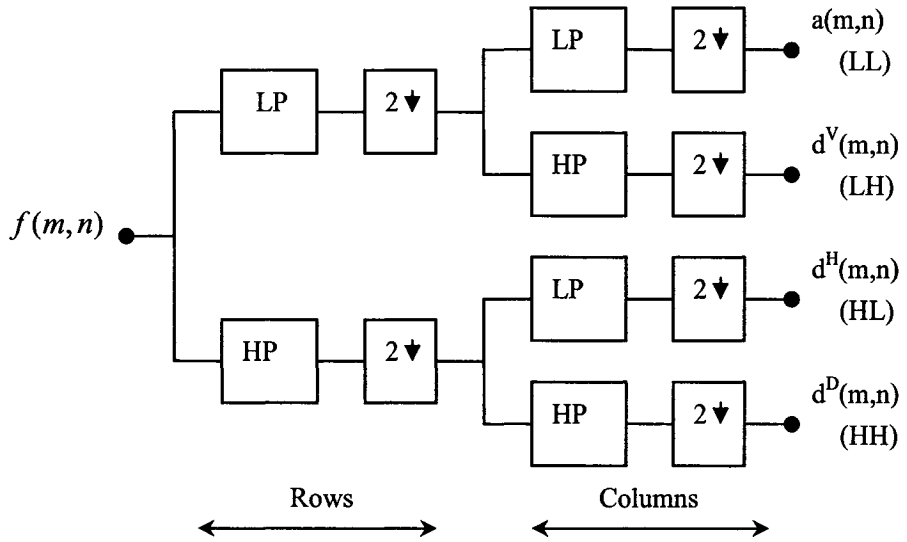

Figure 2.5 A filter bank algorithm for 2-D wavelet transform of image.

Note that this decomposition produces four subband images. The low-frequency subband image (approximations) is further decomposed at the subsequent decomposition level into another four subband images using the same filter bank algorithm as discussed above. One may continue such decompositions for a number of levels until a very fine resolution can be achieved in the low-frequency component of the

image. The two-level image decomposition mechanism is shown in Figure 2.6.

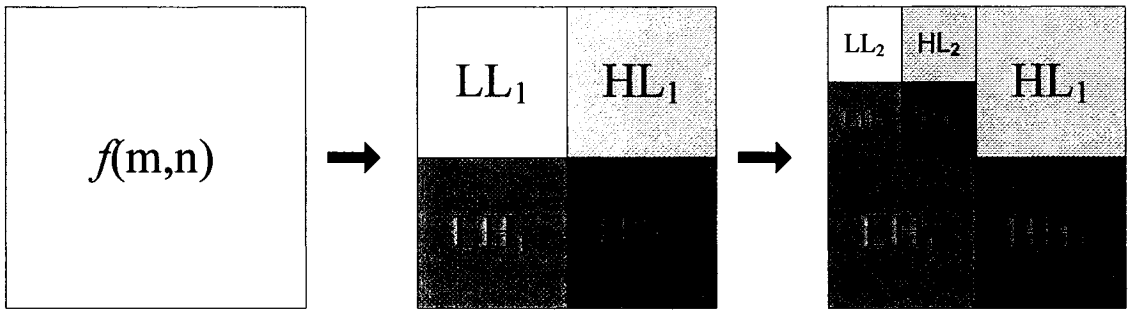

Figure 2.6 The 2-D wavelet transform with two-level decomposition.

2.3 Orthonormal Wavelet Based Filters

2.3.1 Orthonormal Wavelets

From the discussion in section 2.2.3, if $\varphi_{j,k}$ and $\psi_{j,k}$ are orthonormal, i.e.,

$$V_j \perp W_j,$$

$$\langle \varphi_{j,l}, \varphi_{j,l'} \rangle = \delta_{l-l'}$$

$$\langle \psi_{j,l}, \psi_{j',l'} \rangle = \delta_{j-j'}\delta_{l-l'} \qquad \textbf{(2.18)}$$

then (2.13) through (2.15) are valid for orthonormal bases and tight frames alone [3]. Examples of orthonormal wavelets are the family of orthonormal wavelets constructed by Daubechies [8]. The non-symmetrical and compactly supported wavelet is the Symlet-8 wavelets with 8 supporting moments whose scaling and wavelet functions are shown in Figure 2.7.

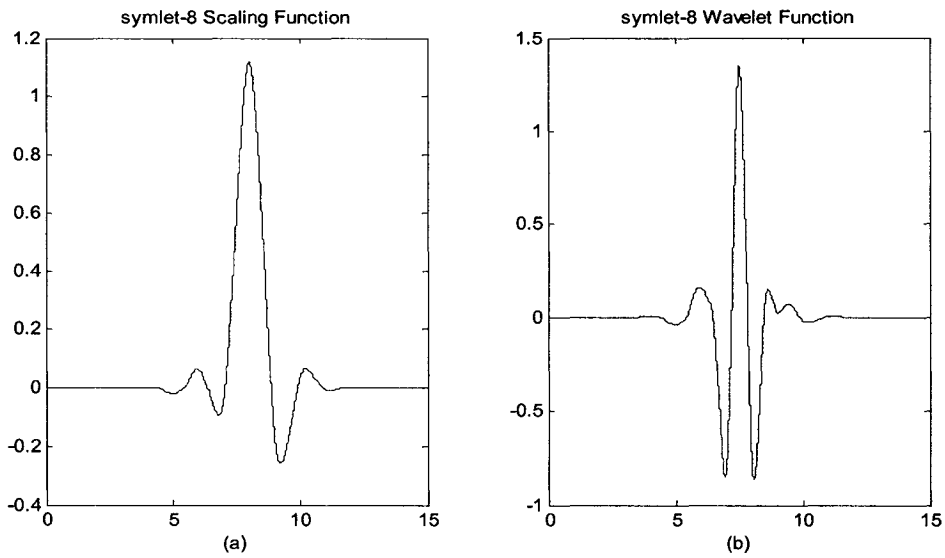

Figure 2.7 Symlet-8 wavelet: (a) scaling function; (b) wavelet function.

2.3.2 Orthonormal Wavelet Based Filters

According to Mallat's herringbone algorithm [29], the FWT resembles the two-band subband coding. Figure 2.8 shows a diagram for one-level image subband decomposition using FWT, where the highest scaling coefficients are samples of the image itself, and $\mathbf{h}_{\varphi}(-n)$ and $\mathbf{h}_{\psi}(-n)$ are the time-reversed version of the scaling and wavelet vectors defined in previous section. Selecting $\mathbf{h}_{\varphi}(n)$ and $\mathbf{h}_{\psi}(n)$ properly such that $\varphi_{j,k}$ determined from (2.5) and (2.6) and $\psi_{j,k}$ from (2.7) and (2.12) satisfy the orthonormal condition (2.18). Moreover, if the scaling and wavelet coefficients also meet the requirement of quadrature-mirror symmetry as given by (2.16), one can obtain an orthonormal wavelet based QMF bank. A compactly supported 8-tap QMF bank, namely, the symlet-8 decomposition and reconstruction filters, are given in Figure 2.9. Note that the analysis and synthesis filters satisfy the perfect-reconstruction condition although

they are not linear-phase.

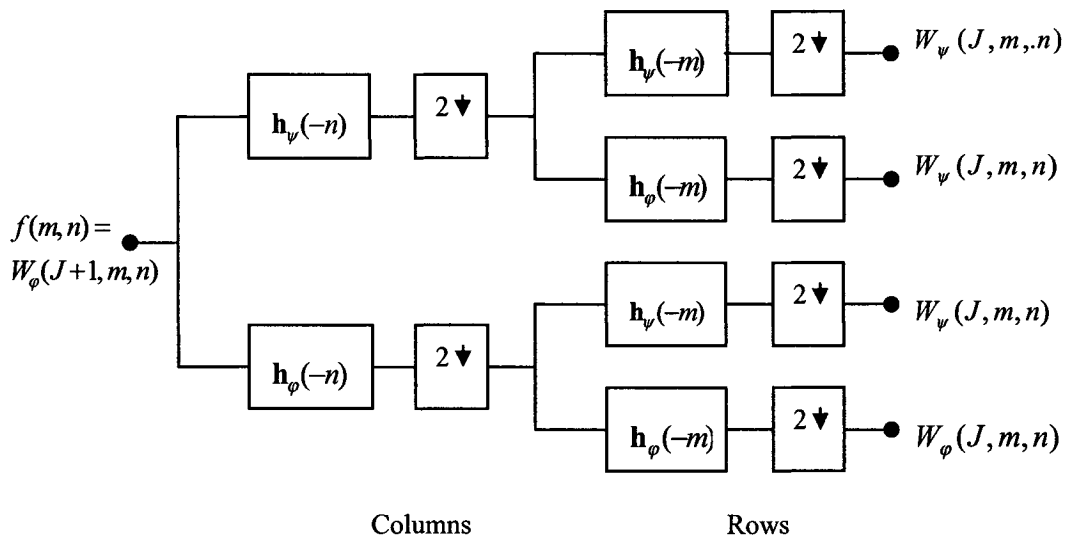

Figure 2.8 A one-level FWT analysis bank for image decomposition.

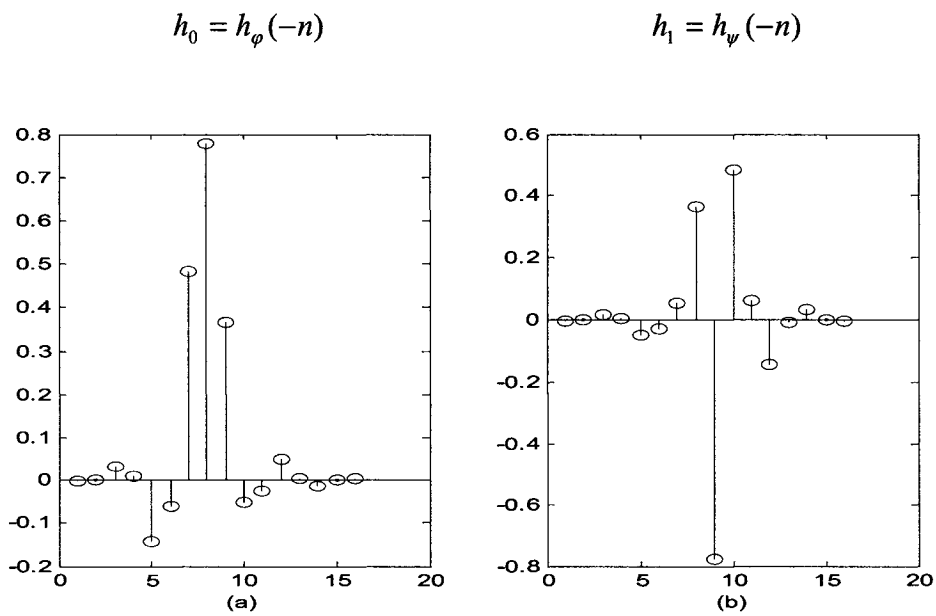

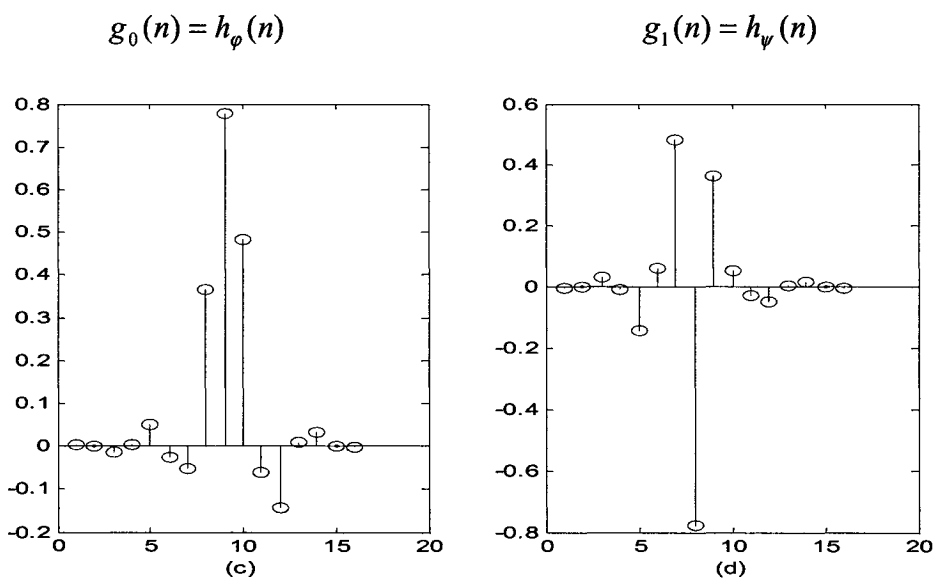

Figure 2.9 8-tap symlet-8: (a) & (b) decomposition filters;

(c) & (d) reconstruction filters.

2.4 Conclusion

In this chapter, we have introduced some background material of wavelet theory, including the basics of wavelets, their important features and constructions. We have reviewed the multi-resolution analysis and wavelet transforms, giving the scaling and wavelet functions used to build wavelet based filter banks. The discrete wavelet transform and its fast implementation have also been discussed for the subband image decomposition. Finally in this chapter, we have shown a class of QMF banks constructed from orthonormal wavelets, which will be used in Chapter 4 for the subband decomposition of images.

Chapter 3

Image Restoration using RCTLS and ARCTLS Algorithms

This chapter presents some image restoration techniques using the regularized constrained total least-square (RCTLS) algorithm and the adaptively regularized constrained total-least square (ARCTLS) scheme. The linear filtering matrix structures as well as fast computations are discussed. A new termination criterion is also proposed in order to increase the convergence speed of the ARCTLS restoration method. Simulation results for the RCTLS and ARCTLS solutions in DFT domain are given at the end of this chapter.

3.1 Basic Mathematics of Image Restoration

3.1.1 Vector-Matrix Formulation of Image Restoration

We can rewrite the degraded image given by (1.1) in a vector-matrix form as

$$\mathbf{g} = \mathbf{H}\mathbf{f} + \mathbf{n} \tag{3.1}$$

where the vectors **f, g** and **n** represent, respectively, the lexicographically ordered original image, degraded image, and additive noise. The matrix **H** represents a linear distortion operator in the discrete form of point spread function (PSF).

Let us consider an image f(m,n) of the size $M \times N$. In a vector form as in (3.1), **f** is presented as a lexicographically ordered column vector, namely,

$$\begin{aligned}\mathbf{f} = [&f_1(0) f_1(1) \cdots f_1(N-1) f_2(0) f_2(1) \cdots f_2(N-1) \\ &\cdots f_M(0) f_M(1) \cdots f_M(N-1)]^T\end{aligned} \tag{3.2}$$

where T denotes the transpose of a matrix or a vector. The vectors **g** and **n** are also column vectors of MN elements generated in a similar fashion to **f**. The **H** is a square circulant matrix of dimension $MN \times MN$ as given below,

$$\mathbf{H} = \begin{bmatrix} \mathbf{H}_0 & \mathbf{H}_{M-1} & \mathbf{H}_{M-2} & \cdots & \mathbf{H}_1 \\ \mathbf{H}_1 & \mathbf{H}_0 & \mathbf{H}_{M-1} & \cdots & \mathbf{H}_2 \\ \mathbf{H}_2 & \mathbf{H}_1 & \mathbf{H}_0 & \cdots & \mathbf{H}_3 \\ \vdots & \vdots & \vdots & \vdots & \vdots \\ \mathbf{H}_{M-1} & \mathbf{H}_{M-2} & \mathbf{H}_{M-3} & \cdots & \mathbf{H}_0 \end{bmatrix} \tag{3.3}$$

Note that **H** consists of M^2 partitions, expressed as $\mathbf{H}_i$ (i=0,1, ... M-1), each being of size $N \times N$. Further, each partition $\mathbf{H}_i$ is obtained from the ith row of $h(m,n)$, i.e.,

$$\mathbf{H}_i = \begin{bmatrix} h(i,0) & h(i,N-1) & h(i,N-2) & \cdots & h(i,1) \\ h(i,1) & h(i,0) & h(i,N-1) & \cdots & h(i,2) \\ h(i,2) & h(i,1) & h(i,0) & \cdots & h(i,3) \\ \vdots & \vdots & \vdots & \vdots & \vdots \\ h(i,N-1) & h(i,N-2) & h(i,N-3) & \cdots & h(i,0) \end{bmatrix} \tag{3.4}$$

The $MN \times MN$ matrix is referred to as block semi-circulant (BSC) of the linear system (3.1) [33]. For simplicity, the notation $\mathbf{H} \in \mathrm{BSC}(M,N)$ is used to indicate that **H** is a BSC matrix of order (M,N).

A dual and equivalent representation of the linear system can be obtained if the input and the output are arranged in an interlaced fashion. If the input vector $\dot{\mathbf{f}}$ is arranged as

$$\dot{\mathbf{f}} = [f_1(0)f_2(0)\cdots f_M(0)f_1(1)f_2(1)\cdots f_M(1); \\ \cdots f_1(N-1)f_2(N-1)\cdots f_M(N-1)]^T \tag{3.5}$$

Then another square matrix $\dot{\mathbf{H}}$ can be obtained,

$$\dot{\mathbf{H}} = \begin{bmatrix} \dot{\mathbf{H}}_{1,1} & \dot{\mathbf{H}}_{1,2} & \cdots & \dot{\mathbf{H}}_{1,N} \\ \dot{\mathbf{H}}_{2,1} & \dot{\mathbf{H}}_{2,2} & \cdots & \dot{\mathbf{H}}_{2,N} \\ \cdots & \cdots & \ddots & \cdots \\ \dot{\mathbf{H}}_{N,1} & \dot{\mathbf{H}}_{N,2} & \cdots & \dot{\mathbf{H}}_{N,N} \end{bmatrix} \tag{3.6}$$

That is, it is circulant at the block level but each $\dot{\mathbf{H}}_{i,j}$ ($1=i,j=N$) is an $M\times M$ matrix. This $NM\times MN$ matrix is referred to as semi-block circulant (SBC) matrix of order (M,N) [33], [34].

3.1.2 Properties of BSC and SBC Matrices and Fast Computation

The BSC and SBC matrices are very important in image restoration. However, it is very time-consuming to carry out a direct computation of BSC and SBC matrices, such as matrix inversion, due to their large size. A great deal of research has been done for efficient computation of these matrices [33], [34]. We will now briefly look into some of the useful properties of BSC and SBC matrices in order to simplify their computation.

First of all, it is noticed that both BSC and SBC matrices are closed under addition, multiplication, and inversion. The size of BSC and SBC is $MN\times MN$, which is very large since most images have usually a few hundreds of pixels in each direction. Therefore, a direct computation of these matrices, especially matrix inversion, becomes very difficult. Fortunately, a fast computation of these large matrices is available in the discrete Fourier transform (DFT) domain.

In the DFT domain, a BSC(M,N) matrix is converted into M^2 block matrices of size $N \times N$. Equivalently, a SBC(M,N) matrix in the DFT domain is transformed into N^2 $M \times M$ block matrices. These $M \times M$ matrices are all zero matrices except for the N block matrices along the diagonal. With this structure, both BSC and SBC matrices can be represented as a spares matrix and thus, a fast and efficient computation can be developed. The details as how to diagonalize the BSC and SBC matrices are given in appendix A.

3.2 RCTLS Algorithm

3.2.1 General

Regularization is a very effective method for solving ill-posed problems [35]. Its basic idea is to use regularization parameters to trade off the fidelity to the observed data for the smoothness of the solution [35], [36], [37].

A large amount of research work has been done to solve (3.1). It is well known that the total least-square (TLS) is an efficient technique to solve a set of noise contaminated linear equations in (3.1) [38], [39]. The constrained total least-squares (CTLS) technique is able to cope well with the case where the noise elements in both **H** and **g** are linearly related and have equal variances [40]. In [41], it has been shown that the regularized constrained total least-squares (RCTLS) is more successful than the CTLS when both **H** and **g** are subject to the same errors which can be modeled as additive Gaussian noise with different statistical properties [14].

We assume that the $N \times 1$ PSF can be represented by

$$\mathbf{h} = \hat{\mathbf{h}} + \Delta\mathbf{h} \tag{3.7}$$

where $\hat{\mathbf{h}}$ and $\Delta\mathbf{h} \in R^N$ are the known and the unknown (error) components of the PSF, respectively. The error component, $\Delta\mathbf{h}$, is modeled as independent and identically distributed (IID) noise with zero-mean and variance σ_h^2.

It is assumed that the observed vector $\mathbf{g}$ is subject to the same error as $\mathbf{H}$ and contaminated by the IID zero-mean additive noise with variance σ_g^2. Furthermore, the noise in the PSF and the observed data are assumed to be uncorrelated. Thus, the degraded image of the vector-matrix form is given by

$$\mathbf{g} = \mathbf{H}\mathbf{f} + \Delta\mathbf{g} \tag{3.8}$$

where $\mathbf{g}, \mathbf{f}, \Delta\mathbf{g} \in R^N$ represent the observed degraded image, the source image and the additive noise in the observed image, respectively, and the $N \times N$ circulant matrix $\mathbf{H}$ can be written as

$$\mathbf{H} = \hat{\mathbf{H}} + \Delta\mathbf{H} \tag{3.9}$$

while $\hat{\mathbf{H}}$ is the known component of $\mathbf{H}$ and $\Delta\mathbf{H}$ is the error part of the PSF matrix, which is constituted by $\Delta\mathbf{h}$ according to (3.7) [42]. Since in most of restoration problems the support region of the PSF is usually much smaller than the actual size of the image, only a very small change in the dimension of the resulting degraded image is caused.

Notice that when the blurring operator is circulant, the error component of the PSF matrix, $\Delta\mathbf{H}$, is also circulant, implying that the elements of $\Delta\mathbf{H}$ are algebraically

related. In [37], Katsaggelos et al have defined an unknown normalized noise vector $\mathbf{u} \in R^{2N}$ consisting of $\Delta\mathbf{h}$ and $\Delta\mathbf{g}$ as shown below,

$$\mathbf{u} = \left[\frac{\Delta h(0)}{\sigma_h}, \cdots, \frac{\Delta h(N-1)}{\sigma_h}, \frac{\Delta g(0)}{\sigma_g}, \cdots, \frac{\Delta g(N-1)}{\sigma_g} \right]^T . \tag{3.10}$$

Here, the region of support for the noise part of the PSF is assumed to be N. But if the supporting region of $\Delta\mathbf{h}$ is M ($M<N$), the remaining N-M components of the noise vector would be zeros. Equations (3.8) and (3.9) can be reformulated as follows,

$$\hat{\mathbf{H}}\mathbf{f} - \mathbf{g} + \Delta\mathbf{H}\mathbf{f} + \Delta\mathbf{g} = 0$$

$$\hat{\mathbf{H}}\mathbf{f} - \mathbf{g} + \mathbf{L}\mathbf{u} = 0 \tag{3.11}$$

where $\mathbf{L}$ is an $N \times 2N$ matrix with the circulant structure, as given below

$$\mathbf{L} = \left[\begin{array}{cccc:c} \sigma_h f(0) & \sigma_h f(N-1) & \cdots & \sigma_h f(1) & \vdots & \\ \sigma_h f(1) & \sigma_h f(0) & \cdots & \sigma_h f(2) & \vdots & \\ \sigma_h f(2) & \sigma_h f(1) & \cdots & \sigma_h f(3) & \vdots & \sigma_g \mathbf{I}_{N\times N} \\ \vdots & \vdots & \ddots & \vdots & \vdots & \\ \sigma_h f(N-1) & \sigma_h f(N-2) & \cdots & \sigma_h f(0) & \vdots & \end{array} \right] \tag{3.12}$$

3.2.2 RCTLS Algorithm

Regularization is one of the most powerful approaches for solving ill-posed problems. In this approach, the recorded data and a priori knowledge are employed in a complementary way [43]. The RCTLS image restoration problem can be rephrased as

$$\min_{\mathbf{f},\mathbf{u}} \left\{ \|\mathbf{u}\|_2^2 + \lambda \|\mathbf{Q}\mathbf{f}\|_2^2 \right\} \tag{3.13}$$

subject to

$$\hat{\mathbf{H}}\mathbf{f} - \mathbf{g} + \mathbf{L}\mathbf{u} = 0 \tag{3.14}$$

where λ is a positive regularization parameter and **Q** is the regularization operator. The role of the regularization operator is two-fold: a) to replace the small eigenvalues of **H** with zero while leaving the large eigenvalues unchanged, and b) to incorporate a prior knowledge about **f** into the restoration process [43], [44].

Equation (3.13) represents a quadratic minimization problem that is subject to a nonlinear constraint due to the term **Lu** in (3.14). A closed-form solution may not exist for the quadratic minimization problem. However, the RCTLS problem in (3.13) and (3.14) can be further simplified by transforming them into an unconstrained optimization problem. First, (3.14) is rewritten as

$$\mathbf{L}\mathbf{u} = -(\hat{\mathbf{H}}\mathbf{f} - \mathbf{g}) \tag{3.15}$$

from which one can obtain

$$\mathbf{u} = -\mathbf{L}^{+}(\hat{\mathbf{H}}\mathbf{f} - \mathbf{g}) \tag{3.16}$$

where $\mathbf{L}^{+}$ is the Moore-Penrose pseudoinverse of **L** [45]. It is easy to see from (3.12) that **L** has a rank of N, leading to

$$\mathbf{L}^{+} = \mathbf{L}^{T}(\mathbf{L}\mathbf{L}^{T})^{-1} \tag{3.17}$$

Substituting (3.16) and (3.17) into (3.13) and noticing that $\|\boldsymbol{A}\|^2=\boldsymbol{A}^{\mathrm{T}}\boldsymbol{A}$, it is easy to see that the minimization of (3.13) is equivalent to the minimization of a nonlinear function defined by

$$P(\mathbf{f}) = (\hat{\mathbf{H}}\mathbf{f} - \mathbf{g})^{T}(\mathbf{L}^{+})^{T}(\mathbf{L}^{+})(\hat{\mathbf{H}}\mathbf{f} - \mathbf{g}) + \lambda(\mathbf{f}^{T}\mathbf{Q}^{T}\mathbf{Q}\mathbf{f}). \tag{3.18}$$

Noting that

$$(\mathbf{L}^{+})^{T}(\mathbf{L}^{+}) = (\mathbf{L}\mathbf{L}^{T})^{-1} \tag{3.19}$$

(3.18) can be rewritten as

$$P(\mathbf{f}) = (\hat{\mathbf{H}}\mathbf{f} - \mathbf{g})^{T}(\mathbf{L}\mathbf{L}^{T})^{-1}(\hat{\mathbf{H}}\mathbf{f} - \mathbf{g}) + \lambda(\mathbf{f}^{T}\mathbf{Q}^{T}\mathbf{Q}\mathbf{f}). \tag{3.20}$$

The above equation represents an unconstrained minimization problem. Therefore, the RCTLS solution of the constrained optimization problem described by (3.13) and (3.14) can be obtained by minimizing P(**f**) in (3.20) with respect to **f.**

3.2.3 RCTLS Solution

It may not be possible to find the minimum of (3.20) in a closed form because of the nonlinearity in the term $(\mathbf{L}\mathbf{L}^{T})^{-1}$. However, it is possible to obtain a solution numerically by iterative optimization algorithms.

By taking the DFT on both sides of (3.20), one can obtain an equivalent minimization problem of P(**f**) as given below (see Appendix B for detail)

$$\min_{F_i}\{P(\mathrm{F}_i)\}, \qquad (\mathrm{i}=0,1\cdots, N-1) \tag{3.21}$$

with

$$P(\mathrm{F}_i) = \frac{\left|\hat{\mathrm{H}}_i\mathrm{F}_i - \mathrm{G}_i\right|^2}{\sigma_h^{\,2}\left|\mathrm{F}_i\right|^2 + \sigma_g^{\,2}} + \lambda\left|\mathrm{Q}_i\right|^2\left|\mathrm{F}_i\right|^2 \tag{3.22}$$

where $|\cdot|$ denotes the modules of a complex quantity. In (3.22), F_i and G_i are the DFT coefficients of the corresponding lower case spatial-domain quantities, $\hat{H}_i$ and Q_i are the eigenvalues of the circulant matrices $\hat{\mathbf{H}}$ and $\mathbf{Q}$, which can be easily obtained using the DFT [42]. The resulting computational reduction is obvious. Equation (3.20) is

decoupled into N equations, each being minimized independently with respect to one DFT coefficient of **f**. Each of these equations still requires solving a vector optimization problem. However, the dimensionality of the problem has been reduced to two, namely, the real and the imaginary parts of the complex DFT coefficient F_i.

3.3 ARCTLS Algorithm

The effectiveness of the RCTLS technique depends on the regularization parameter λ. A high-quality image restoration cannot be guaranteed unless a proper value of λ is selected. For an arbitrary value of λ in the RCTLS method, most of the optimization algorithms including the Davidon-Fletcher-Powell method, may only yield a local minimum but not a global one. The ARCTLS method is able to overcome this difficulty by searching for an appropriate value of λ.

3.3.1 ARCTLS Algorithm in Spatial Domain

The image restoration problem can simply be rewritten in the space domain as

$$\min_{\mathbf{f}} \quad L(\mathbf{f}) \tag{3.23}$$

with

$$L(\mathbf{f}) = \| \mathbf{Hf} - \mathbf{g} \|^2 + \lambda(\mathbf{f}) \| \mathbf{Qf} \|^2 \tag{3.24}$$

where the regularization parameter $\lambda(\mathbf{f})$ depends on the image **f.** The differentiation of $L(\mathbf{f})$ with respect to **f** gives

$$\frac{dL(\mathbf{f})}{d\mathbf{f}} = 2\mathbf{H}^T(\mathbf{Hf} - \mathbf{g}) + \lambda'(\mathbf{f}) \| \mathbf{Qf} \|^2 \tag{3.25}$$

For the sake of simplicity, it has been assumed that $\frac{d(\|\mathbf{Qf}\|^2)}{d\mathbf{f}} = 0$ in obtaining (3.25). In the iterative process, $\lambda(\mathbf{f})$ is adaptively modified in terms of the current estimate of $\mathbf{f}$, e.g., $\hat{\mathbf{f}}$. Setting $\frac{dL(\mathbf{f})}{d\mathbf{f}} = 0$ gives

$$\lambda'(\mathbf{f}) + \frac{2}{\|\mathbf{Q}\hat{\mathbf{f}}\|^2}\mathbf{H}^T(\mathbf{H}\hat{\mathbf{f}} - \mathbf{g}) = 0 \tag{3.26}$$

which implicitly implies a constraint on $\lambda(\mathbf{f})$, i.e.,

$$\lambda'(\mathbf{f})\,|_{\mathbf{H}\hat{\mathbf{f}}=\mathbf{g}} = 0 \tag{3.27}$$

Solving (3.26) with condition (3.27) yields

$$\lambda(\mathbf{f}) = -\frac{2\mathbf{f}^T\mathbf{H}^T(\mathbf{H}\hat{\mathbf{f}} - \mathbf{g})}{\|\mathbf{Q}\hat{\mathbf{f}}\|^2} + C \tag{3.28}$$

where C is a constant. Without loss of generality, one can choose C=0, since the first term on the right-hand side of (3.28) can fully satisfy the condition in (3.27). In order to ensure a numerically stable $\hat{\mathbf{f}}$ and a rigid positive $\lambda(\mathbf{f})$ in the iterative process, it is assumed that

$$\lambda(\mathbf{f}) = \alpha\frac{(\hat{\mathbf{H}}\mathbf{f} - \mathbf{g})^T(\hat{\mathbf{H}}\mathbf{f} - \mathbf{g})}{\mathbf{g}^T\mathbf{g}} \tag{3.29}$$

where $\alpha(>1)$ is an adjustable factor of $\lambda(\mathbf{f})$'s step size. The function $\lambda(\mathbf{f})$ in (3.29) is obviously a quadratic function of $\mathbf{f}$ and describes the proportional relation of the error energy to the observed vector's energy. In each iteration, the regularization parameter $\lambda(\mathbf{f})$ approaches gradually the optimum value when the error energy gets smaller. In the meantime, the correction factor α plays a very important role. Generally speaking the smaller the value of α, the smaller the change of $\lambda(\mathbf{f})$ is in each iteration and the more likely the ARCTLS solution approaches the global optimum. As a result, a high-quality

restored image can be achieved. Conversely, a large value of α yields a faster varying $\lambda(\mathbf{f})$, which may lead to a suboptimal solution and a low-quality restoration. The function $\lambda(\mathbf{f})$ in the ARCTLS scheme is established based on the minimization of the error energy as seen from (3.29). For a given image to be restored, an optimal regularization parameter λ not only exists but also accelerates the convergence of the iterative process.

According to the regularization scheme, a high-quality image restoration can be performed by minimization of the following function,

$$P(\mathbf{f}) = (\hat{\mathbf{H}}\mathbf{f} - \mathbf{g})^T (\mathbf{L}\mathbf{L}^T)^{-1} (\hat{\mathbf{H}}\mathbf{f} - \mathbf{g}) + \lambda(\mathbf{f})(\mathbf{f}^T \mathbf{Q}^T \mathbf{Q}\mathbf{f}). \qquad \textbf{(3.30)}$$

However, it is not realistic to minimize the unconstrained objective function (3.30) due to the following two difficulties [14]:

1) The system of equations structured by $P(\mathbf{f})$ is too large to run in a regular computer. For example, if an $N \times N$ (say 512×512) image is to be restored, the matrix in Equation (3.30) would be of size $N^2 \times N^2$ (262144×262144).
2) $P(\mathbf{f})$ is a high-order nonlinear function of $\mathbf{f}$ because of the involvement of the quadratic function $\lambda(\mathbf{f})$ and the nonlinear elements in $(\mathbf{L}\mathbf{L}^T)^{-1}$. Its first-order derivative is still a high-order nonlinear function. Conventional optimization algorithms cannot assure that the numerical solution of (3.30) is global optimal.

3.3.2 The DFT Domain Solution

The function $P(\mathbf{f})$ given by (3.30) can be simplified by using the diagonalization property of the DFT of circulant matrices [37]. This scheme is able to overcome the first

difficulty mentioned above. However, the second difficulty still remains. In [14], the minimization of $P(\mathbf{f})$ in spatial domain is converted into DFT domain. The minimization problem in the DFT domain can be described as

$$\min_{F_i}\{P(\mathrm{F}_i)\}, \qquad for \quad i=0,1,\cdots,N-1 \tag{3.31}$$

where $P(F_i)$ can be locally linearized at each iteration as

$$P(\mathrm{F}_i^{k+1})=\frac{\left|\hat{\mathrm{H}}_i\,\mathrm{F}_i^{k+1}-\mathrm{G}_i\right|^2}{\sigma_h^2\left|\mathrm{F}_i^k\right|^2+\sigma_g^2}+\lambda(\mathbf{F}^k)\left|\mathrm{Q}_i\right|^2\left|\mathrm{F}_i^{k+1}\right|^2 \qquad for \quad i=0,1,\cdots,N-1 \tag{3.32}$$

with

$$\lambda(\mathbf{F}^k)=\lambda(\mathrm{F}_0^k,\mathrm{F}_1^k,\cdots,\mathrm{F}_i^k,\cdots\mathrm{F}_{N-1}^k). \tag{3.33}$$

In (3.32) and (3.33), k is the index of iteration, F_i and G_i the DFT coefficients of **f** and **g,** respectively, and $\hat{\mathrm{H}}_i$ and Q_i the eigenvalues of the circulant matrices $\hat{\mathbf{H}}$ and **Q**, which can be easily obtained in the DFT domain. As the regularization parameter $\lambda(\mathbf{F})$ in the DFT domain in (3.33) is a function of all DFT coefficients F_i, $(i=0,1,\cdots,N-1)$, it remains the same in each iteration. Moreover, via the local linearization treatment, Equation (3.32) is reduced to a quadratic convex function in each iteration. Performing the first-order derivative and letting it be zero, we can obtain a global optimal solution straightforwardly, so that the second difficulty is tackled. That is, from

$$\frac{\partial P(\mathrm{F}_i^{k+1})}{\partial(\mathrm{F}_i^{k+1})}=0 \tag{3.34}$$

we have

$$F_i^{k+1} = \frac{\hat{H}_i^* G_i}{\left|\hat{H}_i\right|^2 + \lambda(\mathbf{F}^k)\, O(F_i^k)\left|Q_i\right|^2} \qquad (i = 0,1,\cdots,N-1) \tag{3.35}$$

where $\hat{H}_i^*$ is the complex conjugate of $\hat{H}_i$, and

$$\Omega(F_i^k) = \sigma_h^2 \left|F_i^k\right|^2 + \sigma_g^2 \tag{3.36}$$

$$\lambda(F^k) = \frac{\alpha}{E} \sum_{i=0}^{N-1} \left|\hat{H}_i F_i^k - G_i\right|^2 \tag{3.37}$$

with E being the total energy of the observed image as given by

$$E = \sum_{i=0}^{N-1} \left|G_i\right|^2 \tag{3.38}$$

Note that both E and α are constant in the iterative process. The image restoration quality of the above method actually depends on two variables, Ω in (3.36) and λ in (3.37). The main steps in implementing the ARCTLS algorithm are shown below,

Step 1: Initializing F_i^0 and α, i.e., letting $F_i^0 = G_i$ $(i = 0,1,\cdots,N-1)$ and choosing any value of $\alpha > 1$;

Step 2: Computing $\lambda(\mathbf{F}^0)$ using (3.37), or choosing an initial value between 0 and 1;

Step 3: Computing F_i^{k+1} $(i = 0,1,\cdots,N-1)$ using (3.35);

Step 4: Computing $\lambda(\mathbf{F}^{k+1})$ using (3.37);

Step 5: Computing the termination criterion

$$TC = \left|\sum_{i=0}^{N-1} (F_i^{k+1} - F_i^k)\right| \Big/ \left|\sum_{i=0}^{N-1} F_i^k\right|; \tag{3.39}$$

Step 6: Comparing TC with a pre-set small positive number ε, if $TC \geq \varepsilon$, go to step 3; otherwise, terminate iteration.

The program flowchart of the DFT-domain ARCTLS algorithm is given in Figure 3.1.

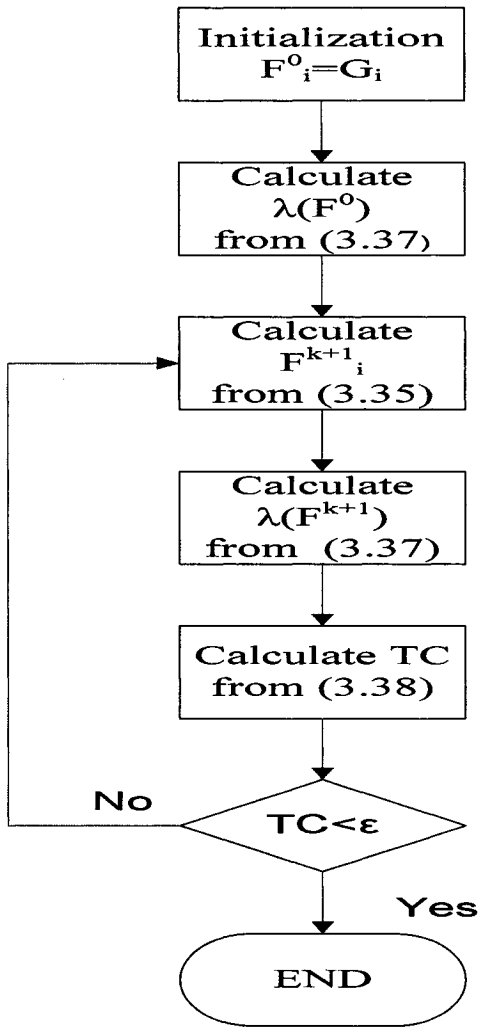

Figure 3.1 Program flowchart of DFT-domain ARCTLS algorithm.

3.3.3 Improvement of Convergence using New Termination Criterion

The ARCTLS algorithm is in general an efficient restoration approach. From our simulation, however, the termination criterion used in step 5 is not optimal. Through extensive experimentations, we have found the following criterion

$$\left\|\mathbf{F}^{k+1}-\mathbf{F}^{k}\right\|_2^2 / \left\|\mathbf{F}^{k+1}\right\|_2^2 < \varepsilon \qquad \textbf{(3.40)}$$

is more reliable and is able to increase the convergence speed. It is noted that the conventional criterion (3.39) uses old DFT coefficients to calculate the error ratio during

entire iteration whereas our new termination criterion makes use of the newly obtained DFT coefficients. It is also to be mentioned that the Euclidean norm has been used in our formula to measure the relative error in each iteration, which is considered as the true and total error. However, the computation implied by (3.39) does not really reflect the total iteration error and therefore, it is not accurate and does not always yield an optimum solution.

3.4 Simulation Results

In this section, the ARCTLS algorithm is simulated and compared with the RCTLS method. The simulation is based on two standard images "Lena" and "Camera-man", both having a size of 256×256. The PSF used to blur the two original images is assumed to be the Gaussian-shaped impulse response,

$$h(i,j) = c \cdot \exp\{-\frac{i^2 + j^2}{2 * \sigma^2}\} \qquad (i,j = 0,1,\cdots,N-1) \qquad \textbf{(3.41)}$$

where c is a constant used to compensate the loss of the distorting system. The discrete Laplacian operator is selected as the regularization operator due to its high-pass characteristic. The Laplacian operator can be expressed as

$$q = \begin{bmatrix} 0 & 1 & 0 \\ 1 & -4 & 1 \\ 0 & 1 & 0 \end{bmatrix} \qquad \textbf{(3.42)}$$

No matter what restoration scheme is used, the observed data are utilized as the initial values in the iterative process. As an objective measurement of the restoration performance for different schemes, the improved signal-to-noise-ratio (*ISNR*) defined as

$$ISNR = 20 \log \frac{\|\mathbf{f} - \mathbf{g}\|_2}{\|\mathbf{f} - \hat{\mathbf{f}}\|_2} \tag{3.43}$$

is employed, where $\mathbf{f}$, $\mathbf{g}$, and $\hat{\mathbf{f}}$, are the original, degraded and restored images, respectively.

3.4.1 Experiment 1 – Lena Image Restoration I

In this experiment, it is assumed that the Gaussian-shaped PSF has a zero-mean and a variance of σ^2 =6.25. Its region of support is set to a square of 29×29 pixels. The PSF is also contaminated by an additive white Gaussian noise (AWGN) of variance $\sigma_h^2 = 8 \times 10^{-7}$ with a support region of 29×29 pixels. The Gaussian noise $\Delta\mathbf{g}$, imposed to the observed image data, has a unit variance.

The original and degraded images are shown in Figure 3.3(a) and Figure 3.3(b), respectively. First, the RCTLS algorithm is used, given the restored image shown in Figure 3.3(c). Images shown in Figure 3.3(d)-(f) are the restored results from the ARCTLS algorithm. Note that in this experiment an arbitrarily chosen initial value of λ is used for ARCTLS iterations. Figure 3.3(d) depicts the restored image obtained from the ARCTLS algorithm with the initial values $\alpha = 10$ and $\lambda_0 = 0.5$. Figure 3.3(e) shows the restored image also resulting from the ARCTLS algorithm but with initial values $\alpha = 10$ and $\lambda_0 = 0.0001$. The last restored image in Figure 3.3(f) is given by the ARCTLS method having $\alpha = 100$ and $\lambda_0 = 0.5$ as initial values.

It should be mentioned that since the linear space-invariant model has been used in this study to degrade the original image, the restored images would in general suffer from the

smoothing of sharp edges and "ringing" artifacts in the vicinity of edges [17]. In addition, our restoration program is implemented with Matlab software package. Whenever convolution or filtering is used, a post-processing of the image boarder is necessary, which can be done by Matlab functions. There are two typical ways to deal with the artifacts around the image boundary. One is to implement a full-size convolution followed by cutting off extra pixels beyond the original image size. Therefore, the filtered image has the same size as the input one as seen from Figure 3.2 (c). The other is to keep the same size as the input image for convolution. As this method may lead to some ringing effect around the image boundary, it is necessary to set the affected pixels to zero. Therefore, the filtered image is slightly smaller than the input one as seen from Figure 3.2 (d) and (e). We have tested the two methods and compared the ISNR values of the restored images in Figure 3.2 (c)-(f) in Table 3.1.

(a)

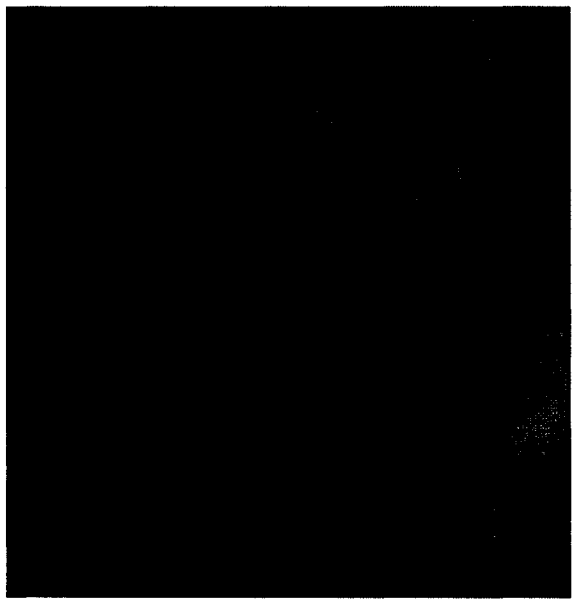

(b)

(c)

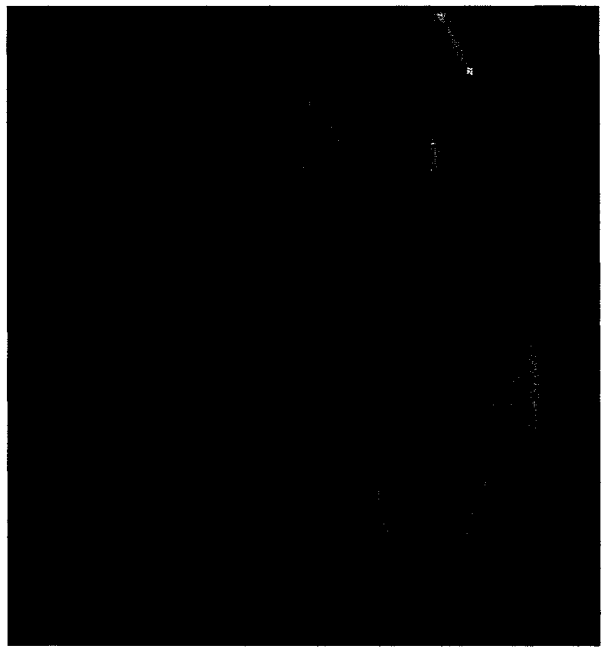

(d)

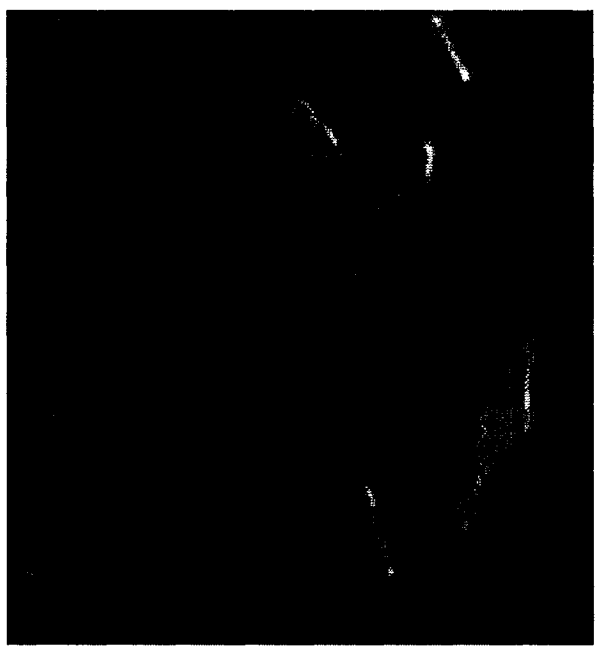

(e)

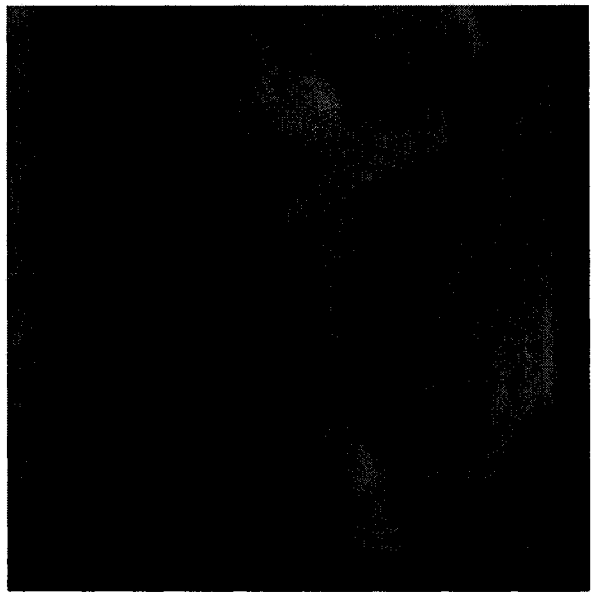

(f)

Figure 3.2 Restoration of "Lena" image using RCTLS and ARCTLS (a)Original image; (b)Degraded image; (c)RCTLS restored image; (d) ARCTLS restored image (α=10,λ_0=0.0001); (e) ARCTLS restored image (α=10,λ_0=0.5); (f) ARCTLS restored image (α=100,λ_0=0.5).

Table 3.1 *ISNR* values of images in Figure 3.2 (c) - (f)

		RCTLS	ARCTLS		
			α =10, λ_0=0.5	α =10, λ_0=0.0001	α =100, λ_0=0.5
ISNR (dB)	Same-size	1.218	4.231	4.228	-3.775
	Full-size	1.025	3.366	3.483	-3.811

It is seen from Table 3.1 that the same-size convolution with boundary pixels set to zero yields a slightly better ISNR. The last column of the table indicates that an improperly chosen α would give a poor restoration result. Table 3.2 shows the regularization parameter λ for the image in Figure 3.2 (d) obtained at each iteration with

respect to the conventional and the proposed termination criterion.

Table 3.2 Regularization parameter λ at each iteration for Figure 3.2 (d)

Iteration	Conventional		Proposed	
	λ_0=0.5	λ_0=0.0001	λ_0=0.5	λ_0=0.0001
1	4.5685×10^{-2}	8.5542×10^{-3}	4.4752×10^{-2}	8.0231×10^{-3}
2	2.8959×10^{-2}	2.1213×10^{-2}	2.7046×10^{-2}	2.2253×10^{-2}
3	2.7078×10^{-2}	2.6053×10^{-2}	2.6545×10^{-2}	2.6786×10^{-2}
4	2.6783×10^{-2}	2.6779×10^{-2}	2.6803×10^{-2}	2.6794×10^{-2}
5	2.6810×10^{-2}	2.6796×10^{-2}		

Although it is difficult from Figure 3.1 to see the difference between the RCTLS and ARCTLS algorithms in terms of the subjective quality of the restored images, our *ISNR* values shown in Table 3.1 have clearly indicated the improvement of the ARCTLS solution over the RCTLS method. In Figure 3.1 (d) and (e), we have selected quite different initial values for λ in the ARCTLS algorithm, and have achieved a final convergence to the optimal values, implying that the ARCTLS is not sensitive to initial values of the regularization parameter. Also, the choice of the adjustable factor α does not seem to affect the convergence. For example, we have selected an improper initial value for α (see the discussion in Section 3.3.1). However, a better *ISNR* value has been obtained by using the ARCTLS method, even though the subjective quality of the restored image is not appreciated. It is clear from Table 3.2 that the proposed termination criterion has yielded a faster convergence of the regularization parameter regardless of its initial values in comparison to the conventional criterion. Actually, the superiority of the proposed termination formula in convergence is evident as reflected by the computation

time. For the restored image in Figure 3.2 (d), the computation time corresponding to the proposed criterion is 9 seconds, while the conventional criterion requires 11 seconds in a Pentium IV PC computer with 1.7GHz processor and 256M memory.

3.4.2 Experiment 2 – Camera-man Image Restoration

Similar to Experiment 1, a Gaussian-shaped PSF with σ^2=6.25 is used. The PSF is supported by a 29×29 square region and is contaminated by AGWN noise with variance $\sigma_h^2 = 8\times10^{-7}$. The observed data are also corrupted by a unit-variance AWGN noise. A 256×256 "camera-man" image as shown in Figure 3.3(a) is selected as the original image for experimentation. Figure 3.3(b) shows the degraded image.

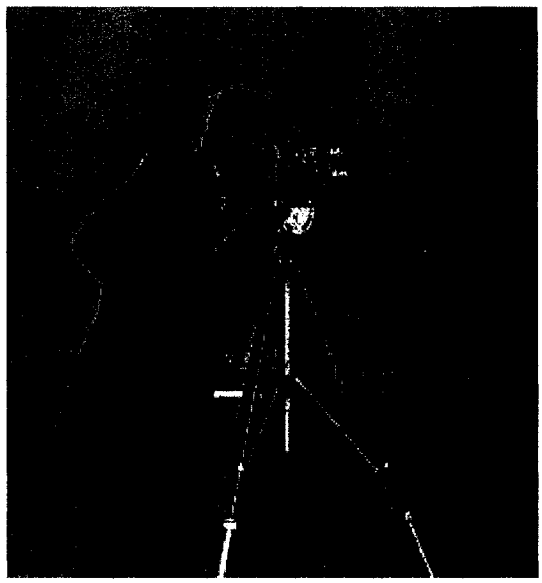

(a)

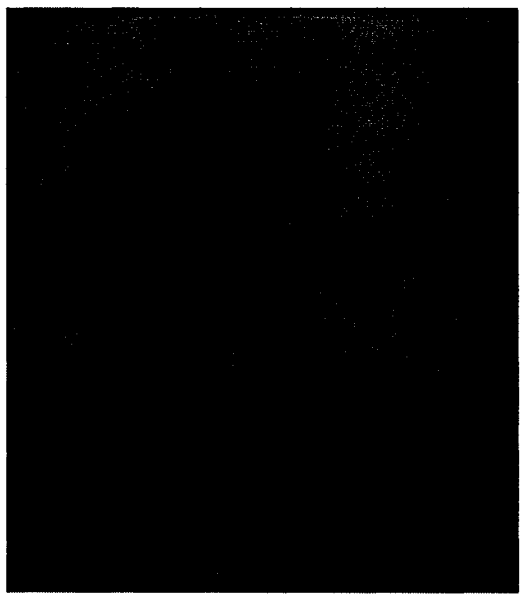

(b)

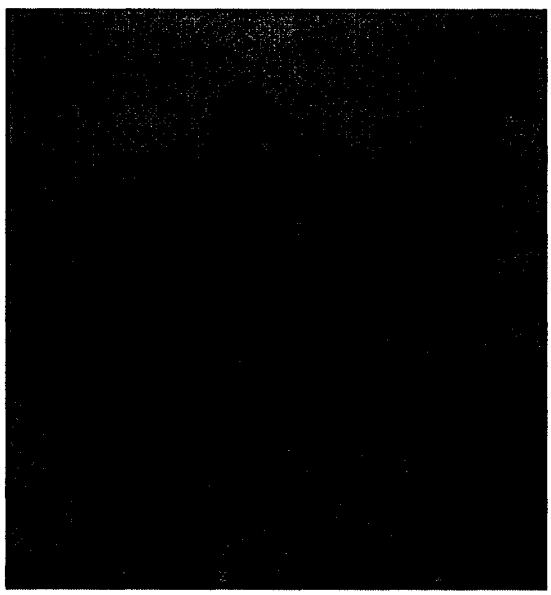

(c)

(d)

Figure 3.3 Restoration of Camera-man image using RCTLS and ARCTLS (a) Original image; (b) Degraded image; (c) RCTLS restored image; (d) ARCTLS restored image with an initial λ calculated from (3.37).

Figure 3.3(c) and (d) show the restored images resulting from the RCTLS and ARCTLS algorithms, respectively. Unlike Experiment 1, the initial value of λ is calculated from (3.37) instead of being chosen arbitrarily. It is seen from this experiment that the ARCTLS gives a better subjective quality than the RCTLS.

3.4.3 Experiment 3 – Lena Image Restoration II

The same image "Lena" as in Experiment 1 is employed. However, it is assumed in this experiment that the variance of the Gaussian-shaped PSF is unknown. This is a more realistic case since the PSF is not exactly known in many applications. We suppose the

realistic case since the PSF is not exactly known in many applications. We suppose the true variance of the PSF is σ^2=9, while the actual variance used in the RCTLS and ARCTLS algorithms is σ^2=16. The support region of the PSF is chosen as 31×31 pixels. The PSF is perturbed by a Gaussian noise with variance $\sigma_h^2 = 2.3 \times 10^{-6}$. An AWGN noise with σ_g^2=0.1 is used to blur the observed image data. The degraded image is shown in Figure 3.4 (a). Figure 3.4 (b) shows the RCTLS restored image. The restoration results from the ARCTLS method with different initial values of λ are shown in Figure 3.4 (c) and (d).

(a)

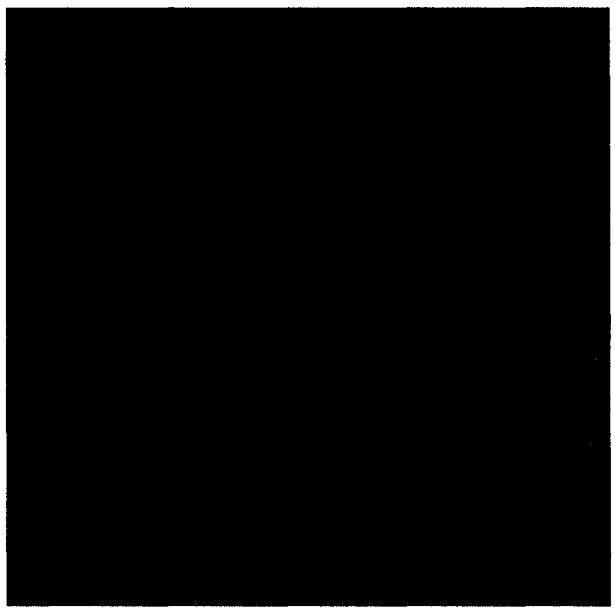

(b)

(c)

(d)

Figure 3.4 Restoration of Lena image with unknown variance of the PSF (a) Degraded image; (b) RCTLS restored image; (c) ARCTLS restored image with λ_0=0.0001; (d) ARCTLS restored image with λ_0 calculated from (3.37).

The *ISNR* values of the restored images are shown in Table 3.3. It is observed from Figure 3.4 and Table 3.3 that the ARCTLS outperforms the RCTLS in both subjective and objective qualities no matter whether the initial value of λ_0 is arbitrarily chosen or calculated from (3.37).

Table 3.3 *ISNR* values of images in Figure 3.4 (b)-(d)

	RCTLS	ARCTLS	
		α =5, λ_0=0.0001	Calculated λ_0
ISNR(dB)	2.271	3.231	3.230

Table 3.4 shows the λ value in each iteration in obtaining the image in Figure 3.4(c) corresponding to the conventional and the proposed termination criteria. Evidently, the proposed criterion leads to a faster convergence.

Table 3.4 Regularization parameter λ at each iteration for Figure 3.4 (c)

Iteration	conventional		our proposed	
	λ_0=0.0001	calculate λ_0	λ_0=0.0001	calculate λ_0
1	4.1564×10^{-4}	8.5542×10^{-3}	4.4752×10^{-4}	4.4645×10^{-4}
2	4.8959×10^{-4}	4.1213×10^{-4}	5.0262×10^{-4}	4.9953×10^{-4}
3	5.0693×10^{-4}	5.0653×10^{-4}		

3.5 Conclusion

In this chapter, we have discussed the RCTLS and ARCTLS algorithms which are known to be very efficient when both the degradation process and the observed image are contaminated by the same type of errors. It has been shown that both RCTLS and ARCTLS problems can be effectively solved in the DFT domain, resulting in a significant reduction in computational complexity. Extensive experimentations have indicated that the ARCTLS method is much better than the RCTLS in terms of *ISNR* although both methods sometimes give similar subjective quality. A new termination criterion has been proposed to increase the convergence rate of the ARCTLS algorithm. It has been shown through computer simulations that the proposed termination criterion is at least 20% faster than the conventional termination criterion.

Chapter 4

Wavelet Domain Image Restoration using ARCTLS

This chapter presents an image restoration approach using wavelet transform in conjunction with the adaptively regularized constrained total least squares (ARCTLS). The matrix representation of 1-D wavelet transform is first formulated for 1-D signal and convolution operator. Then, the matrix representation of 2-D wavelet transform is derived for image and the convolutionnal degradation process. Our objective is to formulate the wavelet transform of image and the 2-D convolution operator properly such that the ARCTLS method can be employed to restore the degraded image in the wavelet domain. Finally, the proposed wavelet domain ARCTLS (WARCTLS) approach is simulated based on some standard images.

4.1 General

In recent years, a lot of work has been done on wavelet domain image restoration. The major advantages of using a wavelet based restoration approach have been described in Chapter 1. Additionally, wavelet transform can be efficiently used to decompose a single-channel linear space-invariant filtering problem into its multichannle counterpart.

This decomposition allows for the processing of a signal or image and the relevant convolution operation in 1-D or 2-D frequency subbands. In this approach, since the convolution operator is also decomposed into several subbands, the cross-subband/channel relations in the observed data can be explicitly taken into account [47].

A general wavelet domain image restoration in the matrix-vector form (3.1) can be rewritten as

$$\mathbf{Wg} = \mathbf{WHW}^T\mathbf{Wf} + \mathbf{Wn}$$

or

$$\hat{\mathbf{g}} = \hat{\mathbf{H}}\hat{\mathbf{f}} + \hat{\mathbf{n}} \qquad \textbf{(4.1)}$$

where $\mathbf{W}$ is the 2-D wavelet transform matrix, $\hat{\mathbf{g}}$, $\hat{\mathbf{f}}$ and $\hat{\mathbf{n}}$ are the vectors representing, respectively, the scaling and wavelet coefficients of the degraded image, those of the original image, and the noise, and $\hat{\mathbf{H}} = \mathbf{WHW}^T$ is the wavelet domain representation of the linear degradation operator.

In the following sections, we will derive the partitioned structure of the wavelet transform matrix $\mathbf{W}$ in order to obtain the subband representation of images and the degradation operator. The derived matrix and vector formulations of the 1-D and 2-D wavelet transforms are necessary for the implementation of the proposed wavelet-domain ARCTLS approach.

4.2 Matrix Representation of Wavelet Transform for 1-D Signal and Convolution Operator

4.2.1 Wavelet-Based 1-D Filter Bank and Matrix Formulation

As shown in Chapter 2, a 1-D signal can be decomposed into two channels by using a filter bank. If the filter bank is derived from a wavelet transform, the two-channel decomposition structure can be redrawn in Figure 4.1, where $\mathbf{W}_L$ and $\mathbf{W}_H$ represent the linear space-invariant wavelet based lowpass and highpass filters, respectively. Here each filtered signal is decimated by two, such that the total number of samples in the output signals is the same as that in the input. The two-channel filtering process can also be expressed

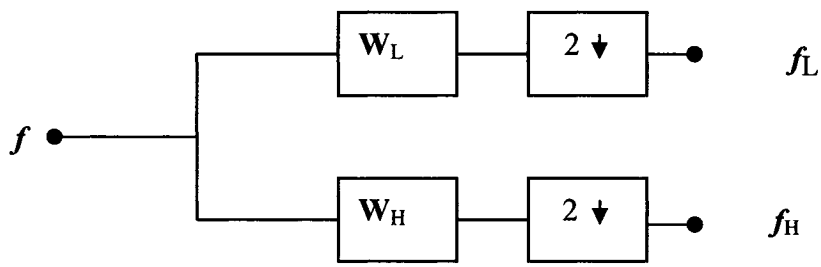

Figure 4.1 Wavelet transform based two-channel decomposition of 1-D signal.

$$\mathbf{Wf} = \mathbf{f}_O \tag{4.2}$$

where $\mathbf{f}$ is an N-dimensional column vector containing the samples of the input signal, $\mathbf{W}$ an $N \times N$ system matrix, and $\mathbf{f}_O$ the output vector containing, in an interlaced fashion, the samples of the decimated lowpass and the highpass filtered signals. In the case of even N, $\mathbf{f}_O$ can be written as

$$\mathbf{f}_O = \left[f_L(0), f_H(0), f_L(1), f_H(1), \cdots, f_L(\frac{N}{2}-1), f_H(\frac{N}{2}-1) \right]^T \tag{4.3}$$

If the coefficients of the impulse responses $\mathbf{W}_L$ and $\mathbf{W}_H$ are denoted as $w_L(i)$ and $w_H(i)$, then $\mathbf{W}$ is a SBC($2, \frac{N}{2}$) matrix as given by

$$\mathbf{W} = \begin{bmatrix} w_L(0) & w_L(1) & w_L(2) & w_L(3) & \cdots & w_L(N-2) & w_L(N-1) \\ w_H(0) & w_H(1) & w_H(2) & w_H(3) & \cdots & w_H(N-2) & w_H(N-1) \\ w_L(N-2) & w_L(N-1) & w_L(0) & w_L(1) & \cdots & w_L(N-4) & w_L(N-3) \\ w_H(N-2) & w_H(N-1) & w_H(0) & w_H(1) & \cdots & w_H(N-4) & w_H(N-3) \\ \cdot & \cdot & \cdot & \cdot & \cdots & \cdot & \cdot \\ \cdot & \cdot & \cdot & \cdot & \cdots & \cdot & \cdot \\ \cdot & \cdot & \cdot & \cdot & \cdots & \cdot & \cdot \\ w_L(2) & w_L(3) & w_L(4) & w_L(5) & \cdots & w_L(0) & w_L(1) \\ w_H(2) & w_H(3) & w_H(4) & w_H(3) & \cdots & w_H(0) & w_H(1) \end{bmatrix} \tag{4.4}$$

In what follows, we will introduce a de-interlacing transform matrix to re-order the output signal vector such that its low-frequency and high-frequency components are separated.

4.2.2 Output Ordering using De-interlacing Matrix

Let the re-ordered version of $\mathbf{f}_O$ be given by

$$\begin{aligned} \tilde{\mathbf{f}} &= [f_L(0), \ f_L(1), \ \cdots, \ f_L(\frac{N}{2}-1), \ f_H(0), \ f_H(1), \ \cdots, \ f_H(\frac{N}{2}-1)]^T \\ &= [\mathbf{f}_L^{\ T}, \mathbf{f}_H^{\ T}]^T \end{aligned} \tag{4.5}$$

where $\mathbf{f}_L$ and $\mathbf{f}_H$ are $\frac{N}{2}$-dimensional vectors containing the re-ordered samples of the decimated lowpass and highpass output signals, respectively. It is easy to see that $\tilde{\mathbf{f}}$ can be expressed as

$$\tilde{\mathbf{f}} = \mathbf{D}\mathbf{f}_O \tag{4.6}$$

where $\mathbf{D}$ is an $N \times N$ orthogonal matrix as given by

$$\mathbf{D} = \begin{bmatrix} 1 & 0 & 0 & 0 & \cdot & \cdot & 0 & 0 \\ 0 & 0 & 1 & 0 & \cdot & \cdot & 0 & 0 \\ 0 & 0 & 0 & 0 & \cdot & \cdot & 0 & 0 \\ \cdot & \cdot & \cdot & \cdot & \cdot & \cdot & \cdot & \cdot \\ \cdot & \cdot & \cdot & \cdot & \cdot & \cdot & \cdot & \cdot \\ 0 & 0 & 0 & 0 & \cdot & \cdot & 0 & 0 \\ 0 & 0 & 0 & 0 & \cdot & \cdot & 1 & 0 \\ 0 & 1 & 0 & 0 & \cdot & \cdot & 0 & 0 \\ 0 & 0 & 0 & 1 & \cdot & \cdot & 0 & 0 \\ \cdot & \cdot & \cdot & \cdot & \cdot & \cdot & \cdot & \cdot \\ \cdot & \cdot & \cdot & \cdot & \cdot & \cdot & \cdot & \cdot \\ 0 & 0 & 0 & 0 & \cdot & \cdot & 0 & 0 \\ 0 & 0 & 0 & 0 & \cdot & \cdot & 0 & 1 \end{bmatrix} \begin{matrix} 0 \\ 1 \\ 2 \\ \cdot \\ \cdot \\ \cdot \\ N/2-1 \\ N/2 \\ \cdot \\ \cdot \\ \cdot \\ N-2 \\ N-1 \end{matrix} \tag{4.7}$$

It is obvious that

$$\mathbf{D}\mathbf{D}^T = \mathbf{D}^T\mathbf{D} = \mathbf{I} \tag{4.8}$$

where $\mathbf{I}$ is the $N \times N$ identity matrix. In the mean time, the matrix $\mathbf{D}$ should be applied to the input signal vector, i.e.,

$$\mathbf{D}\mathbf{f} = \mathbf{f}_D \tag{4.9}$$

In the next subsection, we will investigate the re-ordered and partitioned form of the wavelet transform matrix $\mathbf{W}$ due to the involvement of matrix $\mathbf{D}$.

4.2.3 Matrix Formulation of Wavelet Transform

Pre-multiplying $\mathbf{D}$ on both sides of (4.2) yields

$$\tilde{\mathbf{W}}\mathbf{f}_D = \tilde{\mathbf{f}} \tag{4.10}$$

where $\tilde{\mathbf{W}}$ is given by

$$\tilde{\mathbf{W}} = \begin{bmatrix} \mathbf{W}^E{}_L & \mathbf{W}^O{}_L \\ \mathbf{W}^E{}_H & \mathbf{W}^O{}_H \end{bmatrix} \tag{4.11}$$

The submatrices in (4.11) can be written as

$$\mathbf{W}^{E}{}_{i} = \begin{bmatrix} w_i(0) & w_i(2) & \cdot & w_i(N-2) \\ w_i(N-2) & w_i(0) & \cdot & w_i(N-4) \\ \cdot & \cdot & \cdot & \cdot \\ \cdot & \cdot & \cdot & \cdot \\ w_i(2) & w_i(4) & \cdot & w_i(0) \end{bmatrix} \tag{4.12}$$

$$\mathbf{W}^{O}{}_{i} = \begin{bmatrix} w_i(1) & w_i(3) & \cdot & w_i(N-1) \\ w_i(N-1) & w_i(1) & \cdot & w_i(N-3) \\ \cdot & \cdot & \cdot & \cdot \\ \cdot & \cdot & \cdot & \cdot \\ w_i(3) & w_i(5) & \cdot & w_i(1) \end{bmatrix} \tag{4.13}$$

For simplicity, the subscript i has been used to represent L or H in (4.12) and (4.13). Note that the submatrices $\mathbf{W}_i^E$ and $\mathbf{W}_i^O$ are $\frac{N}{2}\times\frac{N}{2}$ circulant matrix. However, the matrix $\tilde{\mathbf{W}}$ does not have a circulant structure due to the fact that $\mathbf{W}_L^E \neq \mathbf{W}_H^O$. Actually, it is a $\mathrm{BSC}(2,\frac{N}{2})$ matrix.

4.2.4 Decomposition of Convolution Operator in Wavelet Domain

Ignoring the noise term in (4.1) for the moment, the convolution operation in the wavelet domain can be written as

$$\mathbf{g}_O = \mathbf{W}\mathbf{H}\mathbf{W}^T\mathbf{f}_O \tag{4.14}$$

Note that the matrix $\mathbf{WHW}^T$ is an $\mathrm{SBC}(2,\frac{N}{2})$ matrix due to the fact that it is the product of three $\mathrm{SBC}(2,\frac{N}{2})$ matrices. Also $\mathbf{H}$ is a circulant matrix. Therefore, the computation of these matrices can be simplified in the DFT domain (DFT) as discussed in Chapter 3.

From the discussion in previous subsections, (4.14) can be rewritten in terms of $\tilde{\mathbf{W}}$ as

$$(\tilde{\mathbf{W}}\mathbf{D})\mathbf{g} = (\tilde{\mathbf{W}}\mathbf{D})\mathbf{H}(\mathbf{D}^T\tilde{\mathbf{W}}^T)(\tilde{\mathbf{W}}\mathbf{D})\mathbf{f} \tag{4.15}$$

For the circulant matrix $\mathbf{H}$ representing the convolution of an N-point signal with the

kernel

$$\cdots, h(-2), h(-1), h(0), h(1), h(2), \cdots \tag{4.16}$$

centered at 0, it can be shown that

$$\mathbf{H}_D = (\mathbf{D} \quad \mathbf{H} \quad \mathbf{D}^T) = \begin{bmatrix} \mathbf{H}_{(0)} & \mathbf{H}_{(1)} \\ \mathbf{H}_{(-1)} & \mathbf{H}_{(0)} \end{bmatrix} \tag{4.17}$$

where $\mathbf{H}_{(j)}$ is an $\frac{N}{2} \times \frac{N}{2}$ circulant *BSC* matrix representing the convolution of an $\frac{N}{2}$-dimensional vector with the kernel

$$\cdots, h(j-4), h(j-2), h(j), h(j+2), h(j+4), \cdots \tag{4.18}$$

centered at j. Thus, by using **D,** the convolution operator can be decomposed into a few half-length operators $\mathbf{H}_{(j)}$ constituted by the even and odd-indexed coefficients of the original operator. Re-ordering the elements of $\mathbf{f}$ and $\mathbf{g}$ lead (4.15) to

$$\tilde{\mathbf{g}} = (\tilde{\mathbf{W}}\mathbf{H}_D\tilde{\mathbf{W}}^T)\tilde{\mathbf{f}} = \tilde{\mathbf{H}}\tilde{\mathbf{f}} \tag{4.19}$$

where the re-ordered versions $\tilde{\mathbf{f}}$ and $\tilde{\mathbf{g}}$ can be viewed as the $\tilde{\mathbf{W}}$-domain representations of the original signal and the convolution result, respectively, and $\tilde{\mathbf{H}}$ is the transformed convolution operator. Since $\tilde{\mathbf{H}}$ is also a $BSC(2, \frac{N}{2})$ matrix, it is obvious that the decomposition of **H** can easily be implemented in the DFT domain.

4.3 Matrix Representation of Wavelet Transform for 2-D Signal and Convolution Operator

4.3.1 2-D Wavelet–Based Filter Bank and Matrix Representation

For computational simplicity, the 2-D wavelet decomposition is in general implemented by applying the 1-D decomposition to both horizontal and vertical

directions of an image. For an $N \times N$ input signal, $f(x,y)$, the 2-D decomposition will yield four subband signals of size $\frac{N}{2} \times \frac{N}{2}$, as shown in Figure 4.2.

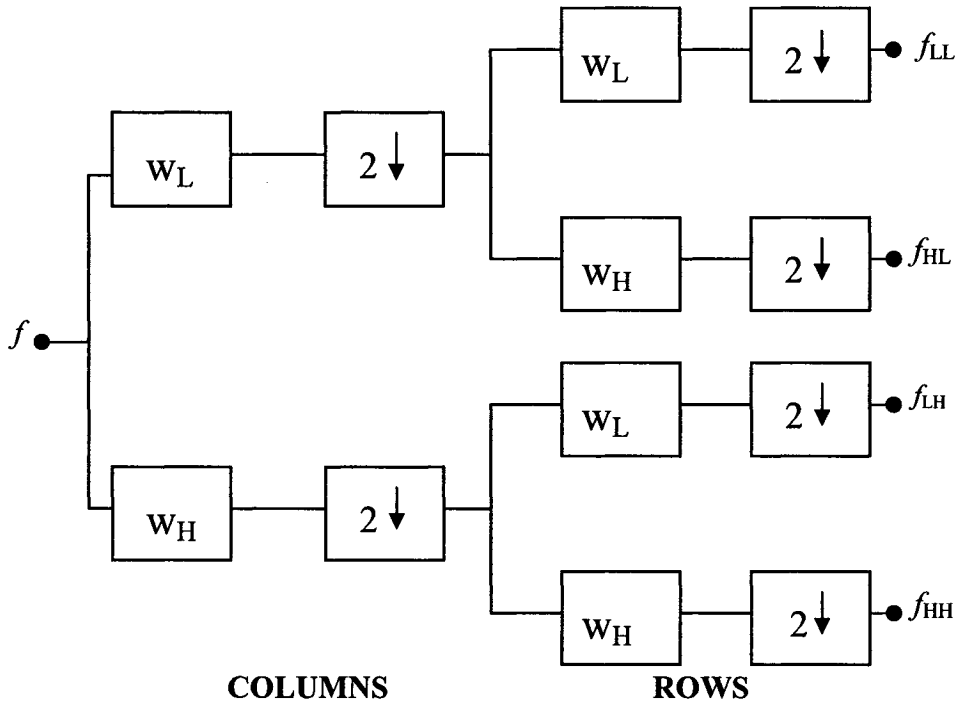

Figure 4.2 Four channel 2-D wavelet-based decomposition filter bank.

We would now like to formulate the matrix-vector representation for the filtering operations in Figure 4.2. If a lexicographic order by column is used, we can stack the 2-D $N \times N$ signal into a $N^2 \times 1$ vector **f**,

$$\mathbf{f} = [f_1(0) \cdots f_1(N-1) f_2(0) \cdots f_2(N-1) \cdots f_N(0) \cdots f_N(N-1)]^T \qquad \textbf{(4.20)}$$

Then from the general wavelet transform (4.1), our 2-D decomposed output $\mathbf{f}_O$ using above filter bank is given by

$$\mathbf{f}_O = [f(0,0)_{LL} f(0,0)_{HL} f(0,0)_{LH} f(0,0)_{HH}; f(1,0)_{LL} f(1,0)_{HL} f(1,0)_{LH} f(1,0)_{HH};$$
$$\ldots, f(\frac{N}{2}-1,\frac{N}{2}-1)_{LL} f(\frac{N}{2}-1,\frac{N}{2}-1)_{HL} f(\frac{N}{2}-1,\frac{N}{2}-1)_{LH} f(\frac{N}{2}-1,\frac{N}{2}-1)_{HH}]^T$$

(4.21)

Similar to the 1-D decomposition, we need to define an $N^2 \times N^2$ 2-D "de-interlacing" matrix $\mathbf{D}_2$, namely

$$\mathbf{D}_2 = \begin{bmatrix} 1 & 0 & 0 & \cdots & 0 & 0 & 0 & \cdots & \cdots & \cdots & \cdots & 0 & 0 & 0 & \cdots & 0 & 0 \\ 0 & 1 & 0 & \cdots & 0 & 0 & 0 & \cdots & \cdots & \cdots & \cdots & 0 & 0 & 0 & \cdots & 0 & 0 \\ 0 & 0 & 0 & \cdots & 1 & 0 & 0 & \cdots & \cdots & \cdots & \cdots & 0 & 0 & 0 & \cdots & 0 & 0 \\ 0 & 0 & 0 & \cdots & 0 & 1 & 0 & \cdots & \cdots & \cdots & \cdots & 0 & 0 & 0 & \cdots & 0 & 0 \\ 0 & 0 & 0 & \cdots & 0 & 0 & 0 & \cdots & \cdots & \cdots & \cdots & 0 & 0 & 0 & \cdots & 0 & 0 \\ 0 & 0 & 0 & \cdots & 0 & 0 & 0 & \cdots & \cdots & \cdots & \cdots & 0 & 0 & 0 & \cdots & 0 & 0 \\ 0 & 0 & 0 & \cdots & 0 & 0 & 0 & \cdots & \cdots & \cdots & \cdots & 1 & 0 & 0 & \cdots & 0 & 0 \\ 0 & 0 & 0 & \cdots & 0 & 0 & 0 & \cdots & \cdots & \cdots & \cdots & 0 & 1 & 0 & \cdots & 0 & 0 \\ 0 & 0 & 0 & \cdots & 0 & 0 & 0 & \cdots & \cdots & \cdots & \cdots & 0 & 0 & 0 & \cdots & 1 & 0 \\ 0 & 0 & 0 & \cdots & 0 & 0 & 0 & \cdots & \cdots & \cdots & \cdots & 0 & 0 & 0 & \cdots & 0 & 1 \end{bmatrix} \begin{matrix} 0 \\ 1 \\ 2 \\ . \\ . \\ . \\ . \\ . \\ . \\ N^2-2 \\ N^2-1 \end{matrix} \quad \textbf{(4.22)}$$

$$\begin{matrix} 0 & 1 & 2 & \cdots & N & N+1 & \cdots & \cdots & \cdots & \cdots & N^2-2+N & \cdots & N^2-2 & N^2-1 \end{matrix}$$

It is easy to verify that $\mathbf{D}_2^T \mathbf{D}_2 = \mathbf{I}$. Using the de-interlacing matrix to the input and output long vectors, one can obtain

$$\mathbf{f}_D = \left[(\mathbf{f}_{EE})^T, (\mathbf{f}_{OE})^T, (\mathbf{f}_{EO})^T, (\mathbf{f}_{OO})^T \right]^T \quad \textbf{(4.23)}$$

$$\tilde{\mathbf{f}} = \left[(\mathbf{f}_{LL})^T, (\mathbf{f}_{HL})^T, (\mathbf{f}_{LH})^T, (\mathbf{f}_{HH})^T \right]^T \quad \textbf{(4.24)}$$

In (4.23), the four subvectors represent the lexicographically ordered images decimated in the horizontal and vertical directions. For example, $\mathbf{f}_{EO}$ stands for a $\frac{N}{2} \times \frac{N}{2}$ subimage which is obtained by selecting the pixels with even indices in the x direction and odd indices in the y direction from the original image. The subvectors in (4.24) represent the subband images obtained by filtering the original image along the x and y directions. For instance, $\mathbf{f}_{HL}$ is the subimage obtained by highpass filtering in the x direction and lowpass filtering in the y direction of the original image.

4.3.2 2-D Wavelet Matrix Formulation

The 2-D wavelet transform matrix $\tilde{\mathbf{W}}$ can be written as $\tilde{\mathbf{W}} = \tilde{\mathbf{W}}_x \cdot \tilde{\mathbf{W}}_y$, where $\tilde{\mathbf{W}}_x$ and $\tilde{\mathbf{W}}_y$ represent the 1-D filtering in the x and y directions, respectively. Furthermore, $\tilde{\mathbf{W}}_x$ and $\tilde{\mathbf{W}}_y$ each are $N^2 \times N^2$ matrices of the following partitioned form,

$$\tilde{\mathbf{W}}_x = \begin{bmatrix} \mathbf{W}^E{}_{(L,x)} & \mathbf{W}^O{}_{(L,x)} & \mathbf{0} & \mathbf{0} \\ \mathbf{W}^E{}_{(H,x)} & \mathbf{W}^O{}_{(H,x)} & \mathbf{0} & \mathbf{0} \\ \mathbf{0} & \mathbf{0} & \mathbf{W}^E{}_{(L,x)} & \mathbf{W}^O{}_{(L,x)} \\ \mathbf{0} & \mathbf{0} & \mathbf{W}^E{}_{(H,x)} & \mathbf{W}^O{}_{(H,x)} \end{bmatrix} \tag{4.25}$$

$$\tilde{\mathbf{W}}_y = \begin{bmatrix} \mathbf{W}^E{}_{(L,y)} & \mathbf{0} & \mathbf{W}^O{}_{(L,y)} & \mathbf{0} \\ \mathbf{0} & \mathbf{W}^E{}_{(L,y)} & \mathbf{0} & \mathbf{W}^O{}_{(L,y)} \\ \mathbf{W}^E{}_{(H,y)} & \mathbf{0} & \mathbf{W}^O{}_{(H,y)} & \mathbf{0} \\ \mathbf{0} & \mathbf{W}^E{}_{(H,y)} & \mathbf{0} & \mathbf{W}^O{}_{(H,y)} \end{bmatrix} \tag{4.26}$$

where $\mathbf{0}$ is an $\frac{N^2}{4} \times \frac{N^2}{4}$ matrix of zero elements, and the symbol $\mathbf{W}^j_{(i,k)}$ (i=L, H, j=E, O, and k=x, y) have been used for convenience. The matrices $\mathbf{W}^j{}_{(i,x)}$ in (4.25) and $\mathbf{W}^j_{(i,y)}$ in (4.26) can be expressed as

$$\mathbf{W}^j_{(i,x)} = \mathbf{W}^j_i \otimes \mathbf{I} \tag{4.27}$$

$$\mathbf{W}^j_{(i,y)} = \mathbf{I} \otimes \mathbf{W}^j_i \tag{4.28}$$

Where $\otimes$ is the Kronecker product and $\mathbf{I}$ the identity matrix. Note that $\mathbf{W}^j_i$ are $\frac{N}{2} \times \frac{N}{2}$ circulant matrices as given by (4.12) and (4.13). Since $\mathbf{W}^j_{(i,k)}$ are Kronecker product of two $\frac{N}{2} \times \frac{N}{2}$ circulant matrices, they are $\frac{N^2}{4} \times \frac{N^2}{4}$ block-circulant. However, the $N^2 \times N^2$ matrices $\tilde{\mathbf{W}}_x$ and $\tilde{\mathbf{W}}_y$ are not circulant but they are usually referred to as block-block semi-circulant (BBSC) matrix of order $(4, \frac{N^2}{4})$. It is obvious

$\tilde{\mathbf{W}}$ is also a BBSC matrix. These matrices have exactly the same properties as the BSC matrix when the 2-D DFT is used for their computation [48], [37].

4.3.3 Decomposition of 2-D Convolution Operator

In two dimensions, it is easy to perform the decomposition of the block circulant convolution operator **H** using the *BBSC* notation. Assuming that **H** is an $N^2 \times N^2$ block circulant matrix representing the 2-D circular convolution of an $N \times N$ signal with the following mask,

$$\begin{array}{ccccccc} \cdot & & & & & & \cdot \\ \cdot & & & & & & \cdot \\ \cdot & h(-2,2) & h(-1,2) & h(0,2) & h(1,2) & h(2,2) & \cdot \\ \cdot & h(-2,1) & h(-1,1) & h(0,1) & h(1,1) & h(2,1) & \cdot \\ \cdot & h(-2,0) & h(-1,0) & h(0,0) & h(1,0) & h(2,0) & \cdot \\ \cdot & h(-2,-1) & h(-1,-1) & h(0,-1) & h(1,-1) & h(2,-1) & \cdot \\ \cdot & h(-2,-2) & h(-1,-2) & h(0,-2) & h(1,-2) & h(2,-2) & \cdot \\ \cdot & & & & & & \cdot \\ \cdot & & & & & & \cdot \end{array} \tag{4.29}$$

which is centered at (0,0). In a manner similar to the 1-D decomposition case, it can be shown that (4.19) also holds for the 2-D case. Moreover, $\tilde{\mathbf{g}}$ is an $N^2 \times 1$ vector of the same form as $\tilde{\mathbf{f}}$ and $\mathbf{H_D}$ is given by

$$\mathbf{H}_D = \begin{bmatrix} \mathbf{H}_{(0,0)} & \mathbf{H}_{(-1,0)} & \mathbf{H}_{(0,1)} & \mathbf{H}_{(-1,1)} \\ \mathbf{H}_{(1,0)} & \mathbf{H}_{(0,0)} & \mathbf{H}_{(1,1)} & \mathbf{H}_{(0,1)} \\ \mathbf{H}_{(0,-1)} & \mathbf{H}_{(-1,-1)} & \mathbf{H}_{(0,0)} & \mathbf{H}_{(-1,0)} \\ \mathbf{H}_{(1,-1)} & \mathbf{H}_{(0,-1)} & \mathbf{H}_{(1,0)} & \mathbf{H}_{(0,0)} \end{bmatrix} \tag{4.30}$$

where $\mathbf{H}_{(i,j)}$ are $\frac{N^2}{4} \times \frac{N^2}{4}$ block circulant matrices that represent the 2-D circular convolution of an $\frac{N}{2} \times \frac{N}{2}$ 2-D signal with the following mask centered at (i,j)

$$
\begin{array}{ccccc}
 & \cdot & \cdot & \cdot & \\
\cdot & \cdot & \cdot & \cdot & \cdot \\
\cdot & h(i-2,j+4) & h(i,j+4) & h(i+2,j+4) & \cdot \\
\cdot & h(i-2,j+2) & h(i,j+2) & h(i+2,j+2) & \cdot \\
\cdot & h(i-2,j) & h(i,j) & h(i+2,j) & \cdot \\
\cdot & h(i-2,j-2) & h(i,j-2) & h(i+2,j-2) & \cdot \\
\cdot & h(i-2,j-4) & h(i,j-4) & h(i+2,j-4) & \cdot \\
\cdot & \cdot & \cdot & \cdot & \cdot \\
 & \cdot & \cdot & \cdot &
\end{array}
\tag{4.31}
$$

As $\mathbf{H}_D$ and $\tilde{\mathbf{H}}$ are BBSC$(4,\frac{N^2}{4})$ and $\mathbf{D}_2\mathbf{H}\mathbf{D}_2^T$ is BSBC, the computation required by (4.19) can be carried out with block matrices in the DFT domain.

4.4 Image Restoration using ARCTLS in Wavelet Domain

From discussions in the previous section, one can decompose the degraded image and the PSF with the 2-D re-ordered wavelet matrix $\tilde{\mathbf{W}}$, yielding four $\frac{N}{2}\times\frac{N}{2}$ lexicographically ordered images, $\mathbf{g}_{LL}, \mathbf{g}_{HL}, \mathbf{g}_{LH}$, and $\mathbf{g}_{HH}$, and the decomposed PSF comprised of four $\frac{N^2}{4}\times\frac{N^2}{4}$ block circulant matrices representing the 2-D circular convolutions of four $\frac{N}{2}\times\frac{N}{2}$ subband images. Then, we can use the ARCTLS algorithm to restore the four subband images. Finally, using the reconstruction filters in the inverse DWT domain, we get the full size restored image [49].

Following the discussion of higher dimension decomposition in wavelet domain in Chapter 2, there is a potential of using $\tilde{\mathbf{W}}$ to transform a signal-channel restoration problem into a higher-dimension multichannel problem. It should be mentioned that the

more channels used for the decomposition, the smaller the stationary length is assumed. If we transform a four-channel restoration problem into a sixteen-channel one (two-level decomposition), the stationary length is reduced to $\frac{N}{4}$. This is accomplished simply by multiplying the result of each filter bank operation by a matrix containing four smaller $\tilde{\mathbf{W}}$ matrices to produce sixteen subband images. The higher-order subband decomposition of the restoration problem is not addressed in this study due to it higher computational complexity.

4.5 Experimental Results

In this section, we will investigate the performance of the proposed wavelet-domain ARCTLS restoration approach. Simulation of the proposed method and comparison with the conventional RCTLS and ARCTLS techniques are carried out based on two standard test images, "Lena" and "Crowd". Similar to the simulation condition in Chapter 3, each test image is degraded by the Gaussian-shaped PSF with known and unknown variances followed by the addition of the AWGN noise. The wavelet-based Symlet-8 orthonormal quadrature mirror filter (QMF) bank is selected in our simulation.

4.5.1 Lena Image Experiment

The original Lena image has been shown in Figure 3.2(a). Figure 4.4(a) shows the degraded image from the same degradation process as that in Experiment 1 of Chapter 3. The parameters for the PSF and the AWGN noise are summarized in Table 4.1. Four subband images of the degraded Lena obtained from the wavelet filter bank

decomposition are tiled in Figure 4.3(b). Figure 4.3(c) gives the corresponding intermediate restoration result, namely, the ARCTLS restored subband images before the reconstruction of the restored complete Lena in Figure 4.3(d). Figure 4.3(d) depicts the restoration result given by the proposed WARCTLS method.

Table 4.1 PSF and AGWN parameters for Figure 4.3

	Variances	Support Region
σ^2	6.25	29×29
σ_h^2	8×10^{-7}	29×29
σ_g^2	1	29×29

(a)

(b)

(c)

(d)

Figure 4.3 "Lena" image restoration with known variance of PSF (a) Degraded Lena image; (b) Four decomposed components of degraded image; (c) Restored suband images using ARCTLS with α=10, λ_0=0.5; (d) WARCTLS restored image.

It is seen from Figure 4.3(b) and (c) that the use of ARCTLS in the wavelet domain has yielded better restored subband images compared to those before restoration, especially the diagonal detail subimage. Also, the restored complete image as shown in Figure 4.3(d) is much better in both subjective and objective qualities than those shown in Figure 3.2(b) to (f) from the RCTLS and ARCTLS approaches implemented in spatial domain. The *ISNR* value of the image in Figure 4.3(d) is shown under the column of WARCTLS-1 in Table 4.3.

The Lena image is also tested for the PSF with unknown variance. The PSF and

AWGN noise parameters related to the degradation are given in Table 4.2. The degraded image is shown in Figure 4.4(a). Figure 4.4(b) and (c) depict the subband images before and after the restoration using the ARCTLS in the wavelet domain. Finally, Figure 4.4(d) shows the complete restored image when the variance of PSF is assumed as 16 in restoration while the true variance is set to 9. The *ISNR* value is listed as the column of WARCTLS-2 in Table 4.3

Table 4.2 PSF and AGWN parameters for Figure 4.4

	Variances	Support Region
True PSF σ^2	9	31×31
Assumed PSF σ^2	16	31×31
σ_h^2	2.3×10^{-6}	31×31
σ_g^2	0.1	31×31

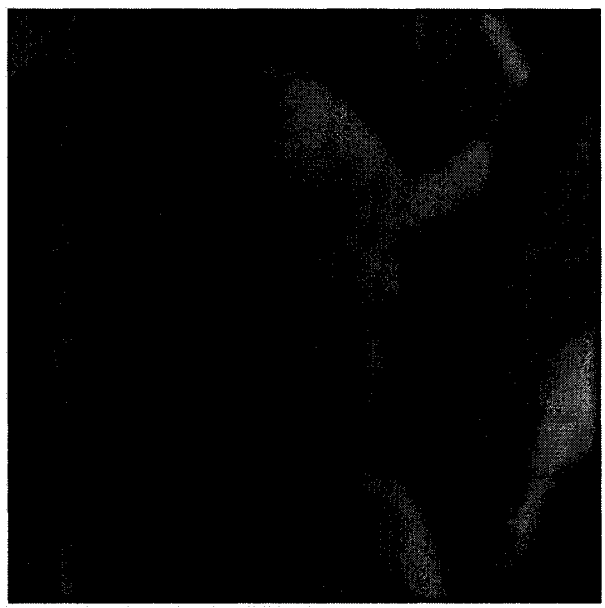

(a)

(b)

(c)

(d)

Figure 4.4 "Lena" image restoration with unknown variance of PSF (a) Degraded Lena image; (b) Four decomposed subband components; (c) WARCTLS restored image; (d) Restored subband images using ARCTLS with $\alpha=10,\lambda_0=0.01$.

Table 4.3 WARCTLS *ISNR* values of Lena image

	WARCTLS-1	WARCTLS-2
ISNR(dB)	8.425	12.658

4.5.2 Crowd Image Experiment

In this experiment, a test image "Crowd" of 512×512 pixels as shown in Figure 4.5 (a)

is used. Similar to the previous experiment, we conduct the restoration for both known and unknown variances of the PSF. The parameters for the degradation process are the same as those used in the previous Lena image experiment (see Table 4.1). The degraded image is shown in Figure 4.5(b). Figures 4.5(c)-(e) depict the restored images resulting from the RCTLS, ARCTLS, and the proposed WARCTLS methods, respectively. Although a subjective judgment of the difference among the three restored images is difficult, yet the *ISNR* values shown in Table 4.4 (see the row of Known Variance) indicate that the WARCTLS method significantly outperforms the RCTLS and ARCTLS methods.

(a)

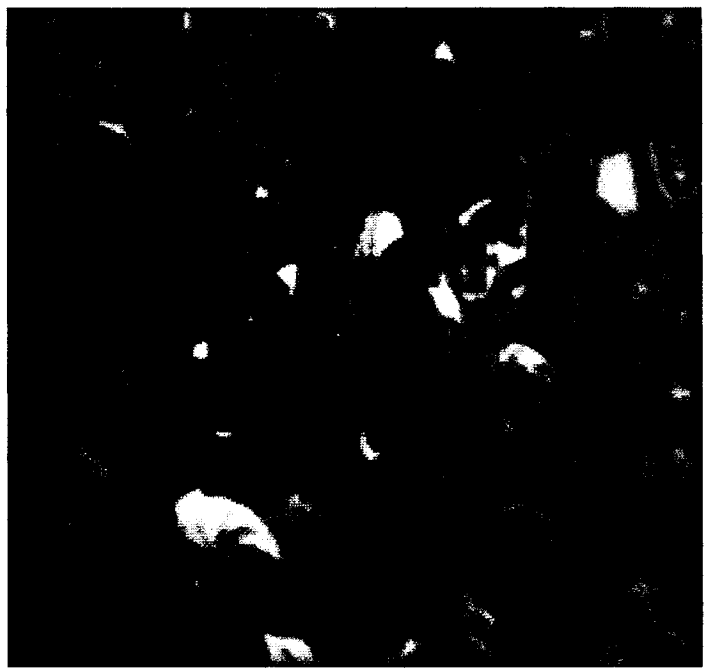

(b)

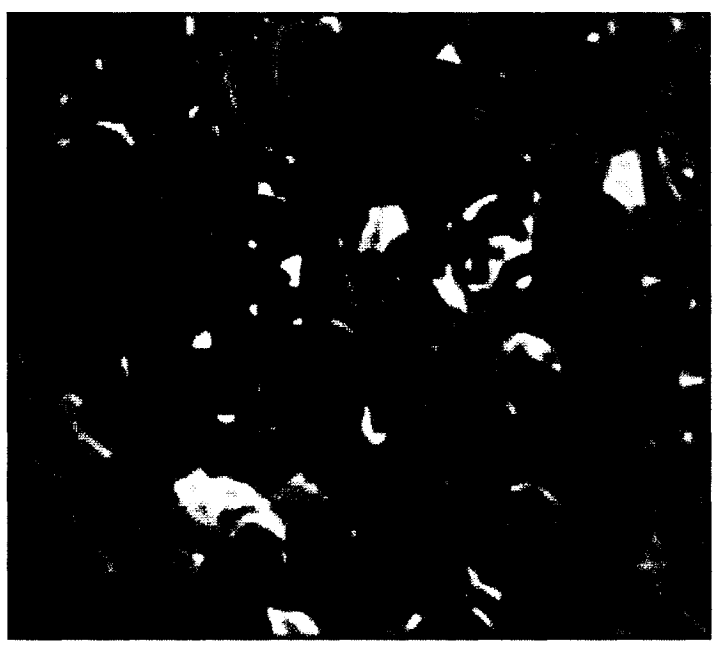

(c)

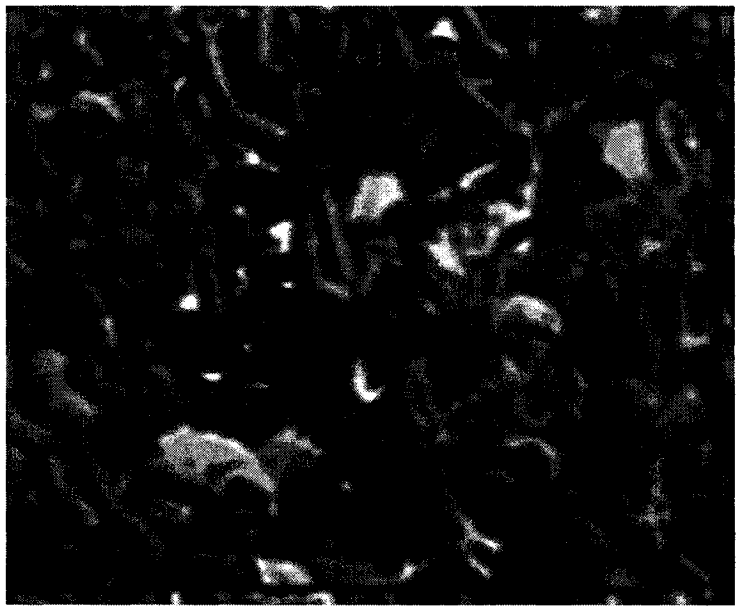

(d)

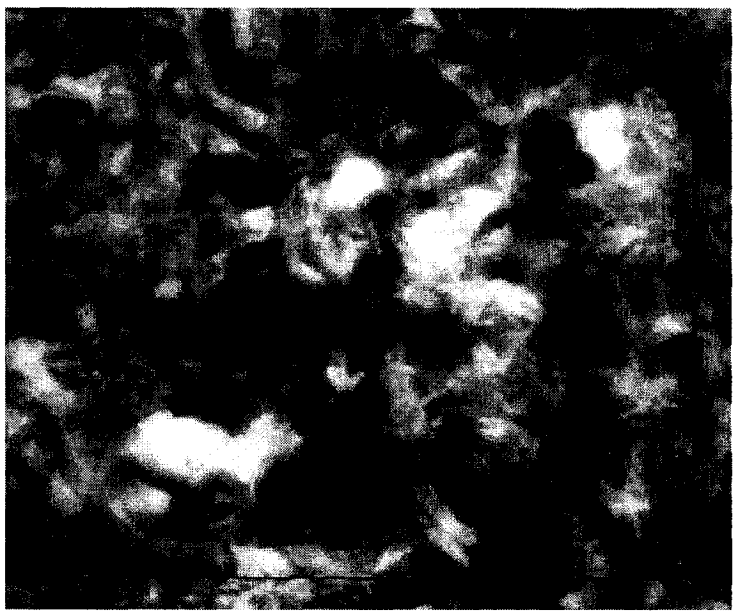

(e)

Figure 4.5 "Crowd" image restoration with known variance of PSF (a) Original image; (b) Degraded image; (c) RCTLS restored image; (d) ARCTLS restored image ARCTLS restored image with $\alpha=5,\lambda_0=0.001$; (e) WARCTLS restored image $\alpha=5,\lambda_0=0.001$.

The restoration of the degraded Crowd image with unknown PSF variance is also performed with the degradation parameters shown in Table 4.2. Figure 4.6(a) shows the degraded image. The relevant restoration results using the RCTLS, ARCTLS, and the proposed WARCTLS methods are depicted in Figure 4.6(b)-(d). The *ISNR* values of these restored images are listed in Table 4.4. It is seen that the *ISNR* given by WARCTLS is much larger than that of the RCTLS and ARCTLS restored images.

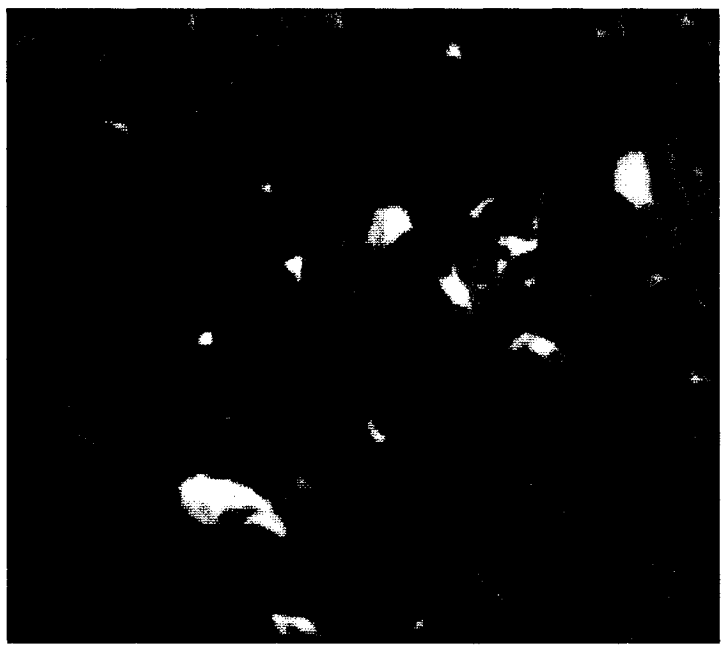

(a)

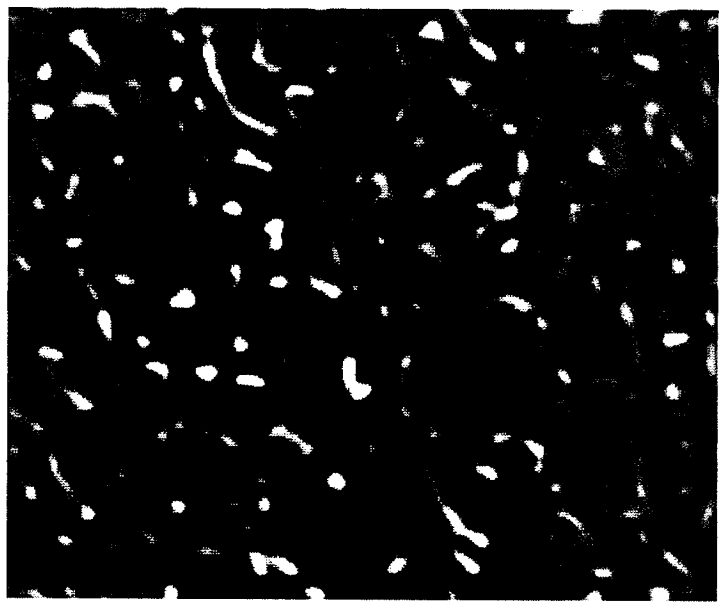

(b)

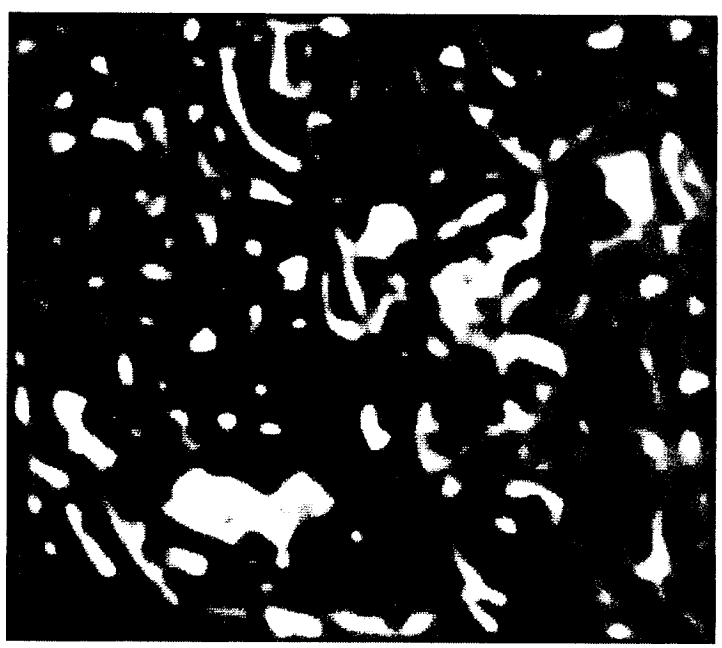

(c)

(d)

Figure 4.6 "Crowd" image restoration with unknown variance of PSF (a) Degraded Crowd image; (b) RCTLS restored image; (c) ARCTLS restored image with α=5 and λ_0 calculated using (3.37); (d) WARCTLS restored image with α=5 and λ_0 calculated using (3.37).

Table 4.4 *ISNR* value of restored "Crowd" image

		RCTLS	ARCTLS	WARCTLS
ISNR (dB)	Known variance experiment	2.98	4.63	8.25
	Unknown variance experiment	-1.17	3.85	10.74

4.6 Conclusion

In this chapter, the matrix representation for the wavelet transform of both 1-D and

2-D signals and convolution operators has been developed and employed to decompose the degraded image as well as the degradation process. The Daubechies symlet-8 wavelet based filter bank has been used for the decomposition of the degraded image and for the reconstruction of the restored subband images. The choice of the symlet-8 wavelet filter bank is motivated by the high regularity of this wavelet, which causes most of the structural information of an image to be projected into the lowest frequency subbands [46]. Two standard images have been used to simulate the proposed WARCTLS method. It has been shown that the WARCTLS method gives a much better *ISNR* for the restored images compared to the spatial-domain RCTLS and ARCTLS techniques. Besides the decomposition of the degraded image in each subband, we have also attempted decomposing the PSF in each subband such that the degraded images can be restored with ARCTLS in each subband. The resulting benefit is that one can chose a different regularization parameter for each subband in the WARCTLS algorithm. By doing so, a significant improvement in both objective and subjective qualities has been achieved.

It is worth-mentioning that we have also carried out restoration experiments by using other orthonormal wavelet filter banks, such as the Daubechies 4-tap filter. Similar restoration results have been obtained, implying that the wavelet-domain restoration performance does not depend on the filter bank used, as long as the perfect reconstruction property is satisfied.

Chapter 5

Conclusion and Future Work

5.1 Conclusion

In this thesis we have investigated digital image restoration techniques using the RCTLS approach in spatial domain and ARCTLS approaches in both spatial domain and wavelet transform domain. Our focus has been on the development of the wavelet domain ARCTLS technique, in which the subband decomposition of the degraded image as well as the degradation process is not straightforward. The work contained in Chapters 3 and 4 constitute the major contribution of the thesis, which can be summarized as follows.

- The DFT-domain solution of the RCTLS and ARCTLS restoration problems has been investigated. It has been shown that the BSC and SBC matrices play a key role in solving these restoration problems. As a lexicographically arranged column vector image is normally used in the image restoration model, the computational complexity increases significantly as the size of the image in question. By using the properties of BSC and SBC matrices in the DFT domain, the computational complexity of the ARCTLS solution has been reduced efficiently. We have also shown that the BBSC and BSSC matrices for the 2-D case share the same structure and property as BSC and SBC matrices.

- It has been shown that the regularization parameters can be used to trade off the fidelity to the observed data for the smoothness of the solution. The ARCTLS method using a regularization parameter has proved more effective in solving ill-posed problems. Our analysis and simulation results show that the ARCTLS is more effective in searching for the optimal regularization parameter, thus assuring a better restored image quality in comparison to the RCTLS.
- In implementing the ARCTLS algorithm, two variables, Ω in (3.36) and λ in (3.37), are the most important parameters which determine the quality of the restored image. The adjustable factor of the step length α is also important for different degraded images, but it is less sensitive to the additive Gaussian noise according to computer simulations. If α is not properly selected, one may get a low-quality restored image.
- To increase the convergence speed of the ARCTRLS algorithm, a new termination criterion has been proposed. The new termination criterion uses Euclidean norm to measure the true total error, and makes use of the newly obtained DFT coefficients in each iteration. Our experimental results have shown that the computational complexity is reduced by at least 20% using the proposed termination formula.
- Matrix representation $\widetilde{\mathbf{W}}$ of wavelet transform for 1-D and 2-D signal decompositions has been presented. With the $\widetilde{\mathbf{W}}$ matrix, we have decomposed the degraded image as well as the convolution operator into subband

counterparts. The ARCTLS algorithm is then applied to each subband image separately, yielding high quality restored subband images and the complete full-band image. Extensive experimentations based on several standard images have shown that the proposed wavelet-domain ARCTLS (WARCTLS) gives a much larger *ISNR* for the restored image compared to the ARCTLS and RCTLS techniques.

5.2 Future Work

Some thoughts concerning future study of the restoration topic have arisen from the completion of this work, these including

- Further optimization of the adjustable factor α in ARCTLS and WARCTLS algorithms – This parameter has been selected through experiment in this thesis. However, in order to guarantee a high quality restoration, α should be determined analytically according to a priori information of the degraded image.
- Restoration of degraded images caused by non-Gaussian-shaped degradation models – This is a more general degradation case where the PSF could be any linear systems and also the additive noise could be non-Gaussian distributed. Therefore, it is necessary to develop the wavelet-domain ARCTLS technique for more general PSF and noisy degradation situations in order to meet the needs of various applications.

- ARCTLS restoration based on higher-level subband image decomposition – In this thesis, only one-level wavelet decomposition of the restored image and the restoration model is considered. One may apply the ARCTLS method to the high-level decomposed subband images and then obtain the complete full-size restored image by reconstructing the subband images at different levels. This higher-level decomposition requires a much higher computational complexity, but it may lead to a better *ISNR* for the restored image.

Appendix A: Diagonalization of SBC Matrix in DFT Domain

An SBC matrix $\mathbf{H} \in SBC(m,n)$ can be reduced to a block diagonal (BD) matrix $\mathbf{D_H}$ by the similarity transformation, $\mathbf{H} = \mathbf{\Omega D_H \Omega^{-1}}$, where $\mathbf{D_H}$ and $\mathbf{\Omega}$ are given by

$$\mathbf{D_H} = \begin{bmatrix} \mathbf{D}_{11} & 0 & \cdots & 0 \\ 0 & \mathbf{D}_{22} & \cdots & 0 \\ \cdots & \cdots & \cdots & \cdots \\ 0 & 0 & \cdots & \mathbf{D}_{NN} \end{bmatrix} \tag{1}$$

with $\mathbf{D}_{ii}$ being an $M \times M$ matrix, $1 \le i \le N$, and

$$\mathbf{\Omega} = \frac{1}{N} \begin{bmatrix} \varepsilon_{0,0}\mathbf{I}_M & \varepsilon_{0,1}\mathbf{I}_M & \cdots & \varepsilon_{0,N-1}\mathbf{I}_M \\ \varepsilon_{1,0}\mathbf{I}_M & \varepsilon_{1,1}\mathbf{I}_M & \cdots & \varepsilon_{1,N-1}\mathbf{I}_M \\ \cdots & \cdots & \cdots & \cdots \\ \varepsilon_{N-1,0}\mathbf{I}_M & \varepsilon_{N-1,1}\mathbf{I}_M & \cdots & \varepsilon_{N-1,N-1}\mathbf{I}_M \end{bmatrix} \tag{2}$$

with $\mathbf{I}_M$ being an $M \times M$ identity matrix and $\varepsilon_{k,l} = \exp\{j(2\pi kl)/N\}$.

We now decompose $\mathbf{\Omega^{-1} H \Omega} = \mathbf{D_H}$ into $\mathbf{E^{-1}H}_{(i,j)}\mathbf{E} = \mathbf{D}_{H(i,j)}$, $(i,j = 1,2,\cdots,M)$, where $H_{(i,j)}$ and $D_{H(i,j)}$ are $N \times N$ matrices containing the (i,j)th elements of H_{lk} and D_{lk} $(l,k = 1,2,\cdots,N)$, respectively. The matrix $\mathbf{E}$ can be written as

$$\mathbf{E} = \frac{1}{N} \begin{bmatrix} \varepsilon_{0,0} & \varepsilon_{0,1} & \cdots & \varepsilon_{0,N-1} \\ \varepsilon_{1,0} & \varepsilon_{1,1} & \cdots & \varepsilon_{1,N-1} \\ \cdots & \cdots & \cdots & \cdots \\ \varepsilon_{N-1,0} & \varepsilon_{N-1,1} & \cdots & \varepsilon_{N-1,N-1} \end{bmatrix} \tag{3}$$

It is easy to verify that $\mathbf{E}^{-1} = \mathbf{E}^{H}$, where H denotes the Hermitian transpose of a matrix or a vector since $\mathbf{E}^{H}$ is the discrete Fourier transform matrix. Furthermore, $H_{(i,j)}$ is circulant since $\mathbf{H}$ is block circulant. Therefore, $\mathbf{D}_{i,j}$ is diagonal and thus $\mathbf{D}$ is block diagonal.

For the sake of convenience, the order of $\mathbf{D}$ is referred to as (P, N) and the sub-matrice

$\mathbf{D}_{kk}$ is called the k-th component of $\mathbf{D}$. Also, $\mathbf{D}(k)$ is interchangeably used with $\mathbf{D}_{kk}$ and the notation $\mathbf{D} \in BD(P,N)$ is used to denote that $\mathbf{D}$ is a BD matrix of order (P,N).

Appendix B: RCTLS Solution in DFT Domain

Let $\mathbf{W}$ be $N \times N$ DFT matrix. Inserting $\mathbf{W}^H\mathbf{W}$ into (3.20), we obtain

$$P(\mathbf{f}) = (\hat{\mathbf{H}}\mathbf{f} - \mathbf{g})^H \mathbf{W}^H \mathbf{W}(\mathbf{L}\mathbf{L}^H)^{-1} \mathbf{W}^H \mathbf{W}(\hat{\mathbf{H}}\mathbf{f} - \mathbf{g}) + \lambda(\mathbf{Q}\mathbf{f})^H \mathbf{W}^H \mathbf{W}(\mathbf{Q}\mathbf{f}) \tag{4}$$

Now, by examining the terms in (4) and using the diagonalization properties of the DFT for circulant matrices, we obtain

$$\mathbf{W}(\hat{\mathbf{H}}\mathbf{f} - \mathbf{g}) = \mathbf{W}\hat{\mathbf{H}}\mathbf{W}^H \mathbf{W}\mathbf{f} - \mathbf{W}\mathbf{g} = \mathbf{D}_{\hat{H}}\mathbf{F} - \mathbf{G} \tag{5}$$

$$(\mathbf{H}\mathbf{f} - \mathbf{g})^H \mathbf{W}^H = [\mathbf{W}(\mathbf{H}\mathbf{f} - \mathbf{g})]^H = (\mathbf{D}_{\hat{H}}\mathbf{F} - \mathbf{G})^H \tag{6}$$

$$\mathbf{W}\mathbf{Q}\mathbf{f} = \mathbf{W}\mathbf{Q}\mathbf{W}^H \mathbf{W}\mathbf{f} = \mathbf{D}_Q\mathbf{F} \tag{7}$$

$$(\mathbf{Q}\mathbf{f})^H \mathbf{W}^H = (\mathbf{W}\mathbf{Q}\mathbf{f})^H = (\mathbf{D}_Q\mathbf{F})^H \tag{8}$$

$$\mathbf{W}(\mathbf{L}\mathbf{L}^H)^{-1}\mathbf{W}^H = [\mathbf{W}(\mathbf{L}\mathbf{L}^H)\mathbf{W}^H]^{-1} = (\mathbf{D}_L)^{-1} \tag{9}$$

where $\mathbf{D}_{\hat{H}}$ and $\mathbf{D}_Q$ and $\mathbf{D}_L$ are given by

$$\mathbf{D}_{\hat{H}} = diag[\hat{\mathbf{H}}_0, \hat{\mathbf{H}}_1, \cdots, \hat{\mathbf{H}}_{N-1}] \tag{11}$$

$$\mathbf{D}_Q = diag[\mathbf{Q}_0, \mathbf{Q}_1, \cdots, \mathbf{Q}_{N-1}] \tag{12}$$

$$\mathbf{D}_L = diag[\sigma_h^2 |\mathrm{F}_0|^2 + \sigma_g^2, \cdots, \sigma_h^2 |\mathrm{F}_{N-1}|^2 + \sigma_g^2]. \tag{13}$$

Having established the above equations, (4) can be rewritten as

$$P(\mathbf{F}) = \sum \{ \frac{|\hat{\mathrm{H}}_i \mathrm{F}_i - \mathbf{G}_i|^2}{\sigma_h^2 |\mathrm{F}_i|^2 + \sigma_g^2} + \lambda |\mathrm{Q}_i|^2 |\mathrm{F}_i|^2 \}. \tag{14}$$

Since each term in the right-hand side of (14) is nonnegative, minimizing it is equivalent

to minimizing each component of the sum, with respect to each frequency, separately. Therefore, the RCTLS solution in the DFT domain can be obtained via

$$\min_{F_i}\{P(\mathrm{F}_i)\}, \qquad \text{for} \quad (i = 0,1,\cdots,N-1) \tag{15}$$

where

$$P(\mathrm{F}_i) = \frac{\left|\hat{\mathrm{H}}_i \mathrm{F}_i - \mathrm{G}_i\right|^2}{\sigma_h^2 \left|\mathrm{F}_i\right|^2 + \sigma_g^2} + \lambda \left|\mathrm{Q}_i\right|^2 \left|\mathrm{F}_i\right|^2 \tag{16}$$

REFERENCES

[1] J. R. Parker, *Algorithms for Image Processing and Computer Vision*, John Wiley& Sons, Inc. New York 1997.

[2] H. C. Andrews, and B. R. Hunt, *Digital Image Restoration,* Englewood Cliffs, New Jersey, 1977.

[3] Gonzalez and Woods, *Digital Image Processing*, Prentice Hall, 2002.

[4] A. K. Katsaggelos, editor, *Digital Image Restoration.* New York: Springer-Verlag, 1991.

[5] G. Anderson and A. Netravali, "Image restoration based on a subjective criterion," *IEEE Trans. Syst., Man, Cybern.*, vol. CMS-6, pp. 845-853, Dec. 1976.

[6] A. K. Katsaggelos et al., "Nonstationary iterative image restoration," *Proc. IEEE ICASSP*, 1985, pp. 696-699.

[7] H. Knutsson, R. Wilson, and G. Granlund, "Anisotropic nonstationary image estimation and its application, part I: Restoration of noisy images," *IEEE Trans. Commun.*, vol. COM-31, no. 3, pp. 388-397, Mar. 1983.

[8] J. W. Woods, "Two-dimensional Kalman filtering," in *Two-Dimensional Digital Signal Processing* I, Topics in Applied Physics, T. S. Huang, Ed. Berlin: Springer, 1981, vol. 42.

[9] F. Jeng and J. W. woods, "Inhomogeneous Gaussian image models for estimation

and restoration," *IEEE Trans. Acoust., Speech, Signal Proc.*, vol. ASSP-36, pp. 1305-1302, Aug. 1988.

[10] F. Jeng and J. W. Woods, "Compound Gauss-Markov random fields for image estimation," *IEEE Trans. Signal Proc.*, vol. 39, pp. 683-697, Mar. 1991.

[11] Gull. S.F, *Development in maximum entropy data analysis, in Maximun Entropy and Bayesian Methods*, Skilling, J. (ed.), Kluwer Academic Publishers, pp. 53-71, 1989.

[12] Richardson, B.H, J. Opt. Soc. Am., 62,55,1972.

[13] Núnez, J. and Llacer, J, "Maximum likelihood estimator and Bayesian reconstruction algorithms with likelihood cross-validation," in: *First Annual Conference on Astronomical Data Analysis Software and System, PASP Conf.* Ser., 25, 20, 1991.

[14] M.G. Kang and A.K. Katassagelos, "General choice of the regularization functional in regularization image restoration," *IEEE Trans. Image Proc.*, vol.4, pp. 594-602, May 1995.

[15] Wufan Chen, Ming Chen and Jie Zhou, "Adaptively regularized constrained total least-squares image restoration" *IEEE Trans. Image Proc.*, vol. 9, pp. 588-596 Apr. 2000.

[16] N. P. Galatsanos, A. K. Katsaggelos and R. T. Chin, A. Hillery, "Least-squares restoration of multichannel images," *IEEE Trans. Signal Proc.*, vol. 39,no. 10, pp. 2222-2236, Oct. 1991.

[17] M.R. Banham, N.P Galatsanos, A.K. Katsaggelos and H. Gonzalez, "Restoration of signle channel images with multichannel filering in the wavelet domain," *Proc. IEEE Int'l. Conf. Syst., Man and Cyber*, pp. 1558-1563, Chicago, IL, Oct. 1992.

[18] J. Bruneau, M. Barlaud, and P. Mathieu, "Image restoration using biorthogonal wavelet transform," *SPIE Conf. Visua l Commun., Image Proc.*, pp. 1404-1415, Nov. 1990.

[19] J. W. Woods and J. Kim, "Image identification and restoration in the subband domain," *Proc. IEEE ICASSP,* Mar. 1992, vol. III, pp. 297-300.

[20] P. Charbonnier, L. Blanc-Féraud, and M. Barlaud, "Noisy image restoration using multiresolution Markov random field," *J. Visual Commun. and Image Rep.*, vol. 3, pp. 338-346, Dec. 1992

[21] I. Daubechies, *Ten Lectures on Wavelets*, Philadelphia: SIAM, 1992.

[22] L. Prasad & S. S. Iyengar, *Wavelet analysis with application to image processing*, CRC Press Boca Raton New York, 1997.

[23] Y. Meyer, *Wavelets: Algorithms and Applications*, SIAM, 1993.

[24] G. Strang, *Wavelets*, American Scientist, 82:250-255, April 1994.

[25] A. Cohen and J. Kovacevic, "Wavelets: the mathematical background," *Proc.*, *IEEE*, 84:514-522, 1996.

[26] S. Mallat, *A Wavelet Tour of Signal Processing*, Academic Press, 1998.

[27] N. H. Nielsen and M. V. Wickerhauser, "Wavelets and time-frequency analysis,"

Proc., IEEE, 84 (4):523-541, April 1996.

[28] S. Mallat, "Wavelet for vision," *Proc. IEEE*, 84(4): 604-614, April 1996.

[29] G. Strang, and V. Strela, "Short wavelets and matrix dilation equations," *IEEE Trans. Signal Proc.*, 43:108-115,1995.

[30] Chui. C. K. *An Introduction to Wavelets*, San Diego: Academic Press, 1992.

[31] Holschneider. M. *Wavelets-An Analysis Tool.* Oxford: Oxford University Press, 1995.

[32] V. Oppenheim and R. W. Schafer, *Discrete-Time Signal Processing*, Pretice Hall, Englewood Cliffs, NJ., 1989.

[33] Mallat. S. G., "A theory for multiresolution signal decomposition: the wavelet representation," *IEEE Trans. Pattern Analysis and Machine Intelligence,* Vol. 11, Issue: 7, July 1989.

[34] Galand, C., Nussbaumer, H., "Quadrature mirror filters with perfect reconstruction and reduced computational complexity," *Proc., IEEE ICASSP'85.*, Vol. 10, pp. 525-528, Apr. 1985.

[35] Smith, M., Barnwell, T., "A procedure for designing exact reconstruction filter banks for tree-structured subband coders," *Proc., IEEE ICASSP'84.*, Vol. 9, pp. 421-424, Mar. 1984.

[36] Vaidyanathan, P.P., Hoang, P.-Q., "Lattice structures for optimal design and robust implementation of two-channel perfect-reconstruction QMF banks," *IEEE Trans. Acoustics, Speech, and Signal Proc.,* Vol. 36, Issue: 1, pp. 81-94, Jan. 1988.

[37] K. T. Lay, *Maximum Likelihood Iterative Image Identification and Restoration*, Ph.D. thesis, Northwestern University, Dec. 1991.

[38] A. K. Katsaggelos, K. T. Lay, and N. P. Galatsanos, "A general framework for frequency domain multichannel signal processing," *IEEE Trans. Image Proc.*, vol. 2, pp. 417-420, July 1993.

[39] A. N. Tikhonov and V. Y. Arsenin, *Solution of Ill-Posed Problems*, Washington, DC: Winston, 1997.

[40] N.P. Galatsanou and A.K. Katsaggelos, "Methods for choosing the regularization parameter and estimating the noise variance in image restoration and their relation," *IEEE Trans. Acoustics, Speech, and Signal Proc.*, vol. 1, pp.322-336, July 1992.

[41] V. Z. Mesarovic, N.P. Galatsanos, and A. K. Katsaggelos, "Regularized constrained constrained total least-squares image restoration," *IEEE Trans. Image Proc.*, vol. 4, pp. 1096-1108, Aug. 1995.

[42] G. H. Golub and C. F. Van Loan, "An analysis of total least-squares problem," *SIAM J.Numer. Anal*, vol. 17, pp. 883-893, 1980.

[43] S.V. Huffel and J. Vandewalle, *The Total Least-Squares Problem.* New York: SIAM, 1991.

[44] T. J. Abatzoglou, J. M. Mendel, and G. A. Harada, "The constrained total least-squares technique and its applications to harmonic superresolution," *IEEE Trans. Signal Proc.,* vol. 39, no. 5, pp. 1070-1087, May 1991.

[45] X. Fan, "The constrained total least squares with regularization and its use in

ill-conditioned signal restoration," Ph.D. thesis, Elec. Comput. Eng. Dep., Mississippi State Univ., Dec. 1992.

[46] B. R. Hunt, "The application of constrained least-squares estimation to image restoration by digital computer," *IEEE Trans. Comput.* Vol. C-22, no. 9, pp. 805-812, Sept. 1973.

[47] M. R. Banham, N. P. Galatsanos, H. Gonzalez and A. K. Katsaggelos "Multichannel Restoration of Single Channel Image Using a Wavelet-Based Subband Decomposition," *IEEE Trans. Image Proc.,* vol. 3, pp. 821-832, Nov. 1994.

[48] N. P. Galatsanos and R. Chin, "Digital restoration of multichannel images," *IEEE Trans. Acoust., Signal Proc.*, vol. 37, pp. 415-421, March 1989.

[49] X. Zhang and W.-P. Zhu, "Wavelet Domain Image Restoration using adaptively regularized constrained total least square," *Proc., IEEE ISIMP2004*, pp.567-570, Oct. 2004, Hong Kong, China.